Peer-reviewed version available at Nanomaterials 2017, 7, 382; doi:10.3390/nano7110382

Review

Engineering the Surface/Interface Structures of Titanium Dioxide Micro and Nano Architectures towards Environmental and Electrochemical Applications

Xiaoliang Wang [1], Yanyan Zhao [2], Kristian Mølhave [3,*] and Hongyu Sun [3,*]

[1] College of Science, Hebei University of Science and Technology, Shijiazhuang 050018, PR China; wxlsr@126.com (X. W.)
[2] Department of Chemistry Boston College Merkert Chemistry Center, 2609 Beacon St., Chestnut Hill, Massachusetts 02467, USA; zhaogh@bc.edu (Y. Z.)
[3] Department of Micro- and Nanotechnology, Technical University of Denmark, Kongens Lyngby 2800, Denmark; kristian.molhave@nanotech.dtu.dk (K. M.); hsun@nanotech.dtu.dk (H. S.)
* Correspondence: kristian.molhave@nanotech.dtu.dk (K. M.); hsun@nanotech.dtu.dk (H. S.); Tel.: +45-45 25 68 40 (H. S.)

Abstract: Titanium dioxide (TiO_2) micro and nano architectures have been intensively studied in the past years because of many varied applications in environmental, energy conversion, and storage fields, such as heterogeneous catalysis, dye-sensitized solar cells, lithium/sodium ion batteries, lithium-sulfur (Li-S) batteries, and bio-nanotechnology, etc. Especially the surface and interface structures in the TiO_2 structures play important roles in those applications. This mini review article focuses on TiO_2 micro and nano architectures with the prevalent crystal structures (anatase, rutile, brookite, and TiO_2(B)), and summarizes major advances in the surface and interface engineering and applications in environmental and electrochemical applications. We present the principles and growth mechanisms of TiO_2 nanostructures via different strategies, with an emphasis on rational control of the surface and interface structures. We further discuss the applications of TiO_2 micro and nano architectures in photocatalysis, lithium/sodium ion batteries, and Li-S batteries. Throughout the discussion, the relationship between the device performance and the surface structures of TiO_2 micro/nano structures will be highlighted. Then we discuss the phase transitions of TiO_2 nanostructures and possible strategies of improving the phase stability. The review concludes with a perspective on the current challenges and future research directions.

Keywords: titanium dioxide; crystal structure; surface/interface structure; photocatalysis; lithium/sodium ion batteries; Li-S batteries; phase stability

1. Introduction

Energy and environment are important factors which affect the sustainable development of the society. Clean energy techniques and environmental treatment solutions based on advanced nanomaterials which are earth abundant and environmentally compatible show the potential to solve the crisis. Titanium dioxide (TiO_2) is such a material that satisfies the criteria [1-2]. As an important and widely used wide bandgap (3.0-3.2 eV) oxide semiconductor, TiO_2 shows unique physical and chemical properties [3]. The applications of TiO_2 materials range from conventional fields (cosmetic, paint, pigment, etc) to functional devices, such as photo- or electrocatalysis, photoelectrochemical or photovoltaic cells, lithium/sodium ion batteries, Li-S batteries, and biotechnological applications [4-13].

There are at least 11 reported bulk or nanocrystalline phases of TiO_2. In nature, TiO_2 forms four main phases: rutile, anatase, brookite, and TiO_2(B). The crystal models of the four structures are

Peer-reviewed version available at Nanomaterials 2017, 7, 382; doi:10.3390/nano7110382

illustrated in Figure 1. All these TiO_2 phases can be viewed as constructed by Ti-O octahedral units. The main structural difference is the connecting ways of the basic Ti-O octahedral repetitive units. For instance, octahedra shares two, three and four edges in rutile, brookite, and anatase phase, respectively. In TiO_2(B) phase, the Ti-O octahedral connection is similar to the anatase one, but with a different arrangement that shows layer character [14]. Under the condition of normal temperature and atmospheric pressure, the relative stability of bulk phase is rutile > brookite > anatase > TiO_2(B) [15]. However, this stability order can be changed by ambient condition and sample properties (particle size, morphology, surface state, etc). The four TiO_2 phases can be distinguished by using diffraction, Raman spectroscopy, or electrochemical techniques. Due to the structural difference, these TiO_2 phases each have their specific applications. Therefore, it is important to study the phase transformation among different phases and develop methods to improve the phase stability[16-18].

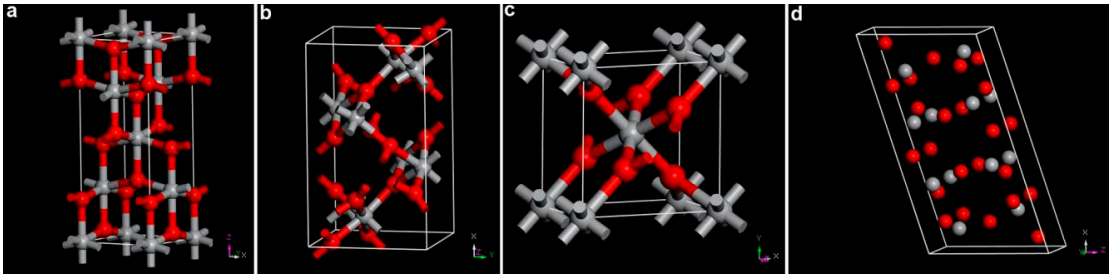

Figure 1. Crystal structures of typical TiO_2 polymorphs: (a) rutile, (b) brookite, (c) anatase, and (d) TiO_2(B). Gray and red spheres are Ti^{4+} and O^{2-} ions, respectively.

For a given TiO_2 phase, the surface and interface structures play important roles in the applications mentioned above [12,13,19]. Photo- or electrocatalysis requires the effective adsorption and desorption of reactant molecules/ions and intermediate products on the surface of TiO_2 photocatalysts [20-23]. The ions transportation is occurred across the surface or interface of TiO_2 electrodes during the continuous charging and discharging processes in lithium/sodium ion batteries[24]. Adjusting the interaction between sulfur cathodes and the surface of TiO_2 host is important to improve the stability of Li-S batteries with a higher capacity than those of lithium ion batteries [25]. Therefore, engineering the surface/interface structures of TiO_2 crystals is not only fundamentally important for studying the essential interaction between molecules or ions and TiO_2 but also valuable to the technical applications [26,27].

In this review, we summarize the most recent progress in engineering the surface/interface structures of TiO_2 micro/nanostructures for the applications in environment and electrochemistry. The article is organized as follows: section 2 reviews the main strategies used for surface/interface engineering in TiO_2 materials; section 3 discusses the advantages and different application of surface/interface engineering in the context of photocatalytic degradation of organic contaminants, water-splitting, CO_2 reduction, electrodes for lithium/sodium ion batteries and Li-S batteries; section 4 analyzes the phase stability of typical TiO_2 structures, and the possible routes to improve the stability; finally, we will provide a personal perspective on the current challenges and important future research directions.

2. Strategies in Surface/Interface Engineering of TiO_2 Micro/Nanostructures

The above discussion shows that surface and interface structures in TiO_2 materials are related to the electronic/optical properties and thus diverse applications ranging from energy to environment. So far, different methods have been proposed to control the surface and interface configurations for TiO_2 micro/nanostructures [28-30]. Among the methods, a primary classification can be made by distinguishing physical and chemical methods, which are based on top-down and bottom-up approaches, respectively. There are several excellent reviews describing the specific synthesis methods (such as self-assembly, template, hydrothermal, solvothermal, annealing,

Peer-reviewed version available at Nanomaterials 2017, 7, 382; doi:10.3390/nano7110382

electrochemical method, etc.) to achieve the control of surface/interface structures [5,19,31]. In this paper, we avoid describing the different synthesis methods, but discuss fundamental strategies, including one-step (sometimes called *in-situ*) methods, post treatment, and theoretical guidance, those are used to engineer the surface/interface structures.

2.1 One-step *approach*

In order to achieve the engineering of the surface/interface structures via the one-step approach, understanding the nucleation and further growth is essential. Up to now, solution-based and vapor-based approaches have been developed to control the nucleation and growth, and different mechanisms including vapor−liquid−solid, orientation attachment, Ostwald ripening, surfactant-controlled, and surface reaction-limited growth have been proposed, which have been covered in a number of excellent reviews [5,19,31].

Richter *et al*. fabricated aligned TiO_2 nanotube arrays by anodic oxidation of a pure titanium sheet in an aqueous solution containing hydrofluoric acid (0.5 ~ 3.5 wt%) [32]. Electron microscopy images showed the tops of the tubes were open, and the bottoms of the tubes were closed. The average tube diameter was found to grow with increasing anodizing voltage, while the length of the tube was found to be independent of anodization time. Field-enhanced void structure was responsible for the formation of the nanotube structures. By suitable choice of the pH value, electrolytes and the Ti sources, the geometry and composition of the nanotube arrays can be controlled more precisely (Figure 2).

Penn *et al*. proposed that some TiO_2 nanostructures can be formed in solution through the route of oriented attachment, where the merger of nanocrystals is based on crystallographic orientations of the nanocrystals to form single crystalline structure [33]. Experiment and simulations showed that the driving force of an oriented attachment growth was the reduction of the surface energy contributed by the removal of certain crystal facets with a high surface energy. The kinetics of the oriented attachment growth was directly related to the solution properties and reaction temperature. Therefore, it is possible to control the surface/interface properties of the final TiO_2 nanostructures by modifying the crystal facets of the pristine nanocrystals as well as solution viscosity and others.

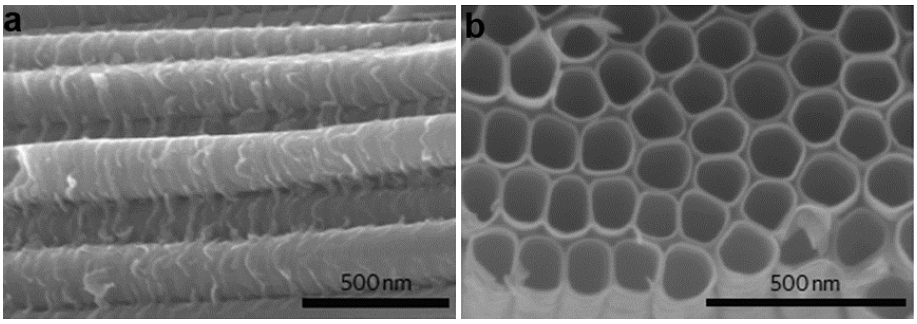

Figure 2. Engineering the surface/interface structures in TiO_2 materials via one step approach. Scanning electron microscopy images of amorphous TiO_2 nanotube arrays fabricated by anodic oxidation. (a, b) reprinted from [32] with permission, Copyright Nature Publishing Group, 2010.

2.2 Post treatment routes

Based on the well-established top-down and bottom-up approaches, the synthesis of TiO_2 micro/nanostructures with controllable parameters, such as size, morphology, composition, as well as assembly, can be achieved. Those TiO_2 materials with well-defined geometry and chemistry provide abundant possibilities to further tune the atomic scale structures. Therefore, different post-treatment techniques, including thermal annealing, electrochemical cycling, and solution reaction, have been developed to yield TiO_2 materials with modified surface and interface structures [34-40].

By employing high pressure (~20 bar) hydrogen annealing treatment, Chen *et al.* successfully converted the pristine white TiO_2 nanoparticles into black hydrogenated particles (Figure 3a-e) [34]. The color change indicated the optical absorption properties had been modified through the treatment. Further structural characterizations showed that the obtained black TiO_2 nanoparticles possessed core-shell structure, which included a well-crystallized lattice core surrounded by a lattice-disordered shell. The surface layer with disordered feature was due to hydrogen dopant, form the Ti–H and O–H bonds, and contributed to the midgap states and the black color of the hydrogenated TiO_2 nanoparticles. Similar to the case of hydrogen treatment, annealing in oxygen deficient atmosphere also results in the effective modification of the surface/interface structures. Huang *et al*. reported a facile solution and subsequent thermal annealing in ethylene for the synthesis of rutile TiO_2 nanoparticles [35]. They found that each particle surface was etched to form pits with an average size of 2–5 nm, which were named as quantum pits. It was believed that the nickel chloride assisted ethylene thermolysis played an important role in the formation of the above novel structure. During the annealing, nickel ions catalyzed ethylene thermolysis to form carbon on the surface of TiO_2 nanoparticles. Then, the carbon layer and trace Cl_2 in the reaction chamber *in situ* etched TiO_2 to form quantum pits according to the reaction: $TiO_2 + 2C + 2Cl_2 \leftrightarrow TiCl_4 + 2CO$. Compared to the nanoparticles with other morphologies, the obtained rutile TiO_2 nanoparticles with quantum pits possess more unsaturated bond and other defect structures, such as terraces, steps, and kinks, which will provide more active sites for lithium ions storage and enhance the conductivity. Recently, electrochemical cycling in different mediums (aqueous, organic solution, and ionic liquids) have been employed to modify the surface structure and composition of TiO_2 materials. The results show that the surface defect structures, especially oxygen vacancies, and their amount can be well controlled by tuning the electrochemical parameters at ambient conditions.

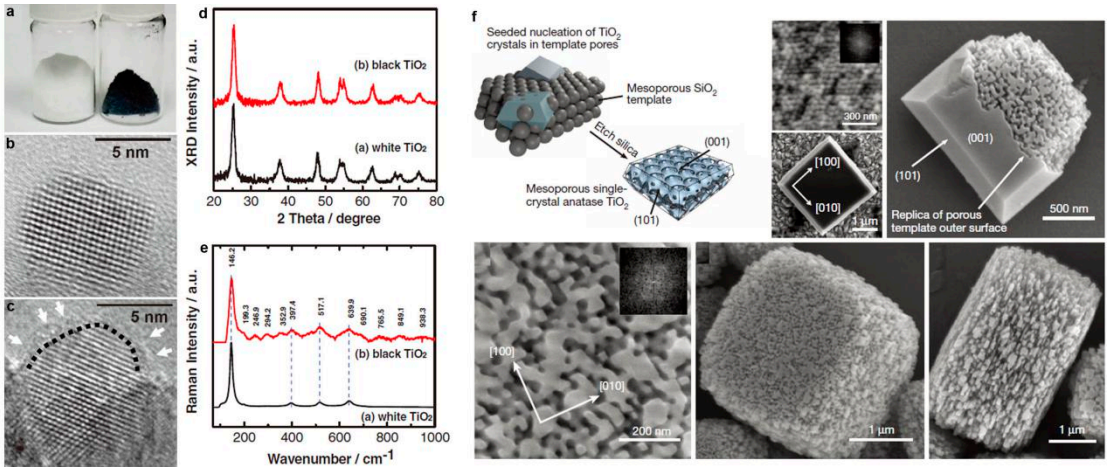

Figure 3. Post treatment route to tune the surface/interface structures in TiO_2 materials. (a) A photo comparing unmodified white and disorder-engineered black TiO_2 nanocrystals; (b, c) HRTEM images of TiO_2 nanocrystals before and after hydrogenation, respectively. In (c), a short dashed curve is applied to outline a portion of the interface between the crystalline core and the disordered outer layer (marked by white arrows) of black TiO_2; (d, e) X-ray Diffraction (XRD) and Raman spectra of the white and black TiO_2 nanocrystals (reprinted from [34] with permission, Copyright American Association for the Advancement of Science, 2011). (f) Schematic and electron microscopy images of mesoporous single-crystal nucleation and growth within a mesoporous template (reprinted from [29] with permission, Copyright Nature Publishing Group, 2013).

Template assistance is also effective to control the surface/interface of TiO_2 micro/nano configurations. Crossland *et al*. developed a mesoporous single-crystal anatase TiO_2 based on seeded nucleation and growth inside a mesoporous template immersed in a dilute reaction solution (Figure 3f) [29]. In a typical process, silica template was firstly seeded by pre-treatment in a solution of $TiCl_4$ at 70 °C for 60 min. The anatase TiO_2 mesoporous single-crystal was obtained via hydrothermal

Peer-reviewed version available at Nanomaterials 2017, 7, 382; doi:10.3390/nano7110382

treatment of TiF_4 in the presence of hydrofluoric acid and pre-treated silica template. The template was removed by etching in aqueous NaOH to recover the mesoporous TiO_2 crystal product. The final product reveals facet truncated bipyramidal crystals with external symmetry matching that of the homogeneously nucleated bulk crystals, whose mesoscale structure is a negative replica of the silica template. Compared to the conventional TiO_2 nanocrystalline, the TiO_2 mesoporous single-crystal show higher conductivity and electron mobility.

2.3 Theoretical guidance

With the rapid development of modern calculation and simulation, computational material methods based on diverse scale, such as finite element, large scale molecular dynamics (MD) simulation, and density functional theory (DFT) are becoming more and more powerful to provide fundamental insights into experimental results, and more importantly, design and predict the performance of novel functional materials. With the assistance of theoretical methods, it is possible to understand the nucleation, growth, surface properties in liquid and gas environment, which is important to achieve controllable synthesis and optimize physical/chemical properties of the nanomaterials [41-43].

The equilibrium morphology of a crystal is given by the standard Wulff construction, which dependents on the surface/interface properties. Barnard and Curtiss investigated the effects of surface chemistry on the morphology of TiO_2 nanoparticles by using a thermodynamic model based on surface free energies and surface tensions obtained from DFT calculations. In the condition of hydrated, hydrogen-rich, and hydrogenated surfaces, the shape of anatase and rutile nanoparticles vary little, however, in the case of hydrogen-poor and oxygenated surfaces, the anatase and rutile nanocrystals become elongated. The results show that the exposed facets of the TiO_2 nanocrystals can be controlled through modifying the surface acid-base chemistry.

Besides the acid-base condition, heterogeneous atoms or surfactant adsorption can also affect the surface and interface structures. Based on DFT calculations, Yang *et al*. [28] systematically studied the adsorption of a wide range of heterogeneous non-metallic atoms X (X = H, B, C, N, O, F, Si, P, S, Cl, Br or I) on {100} and {101} facets of anatase TiO_2 crystals (Figure 4). The results show the adsorption of F atoms not only decreases the surface energy for both the (001) and (101) surfaces, but also results in the fact that (001) surfaces are more stable than (101) surfaces, i.e., the F adsorption is favorable for the formation of (001) facets in anatase TiO_2. The theoretical results inspire intense studies on the surface structure control of TiO_2 crystals. Experimentally, a mixture containing titanium tetrafluoride (TiF_4) aqueous solution and hydrofluoric acid was hydrothermally reacted, to generate the truncated anatase bipyramids, and anatase TiO_2 single crystals with a high percentage of {001} facets were obtained.

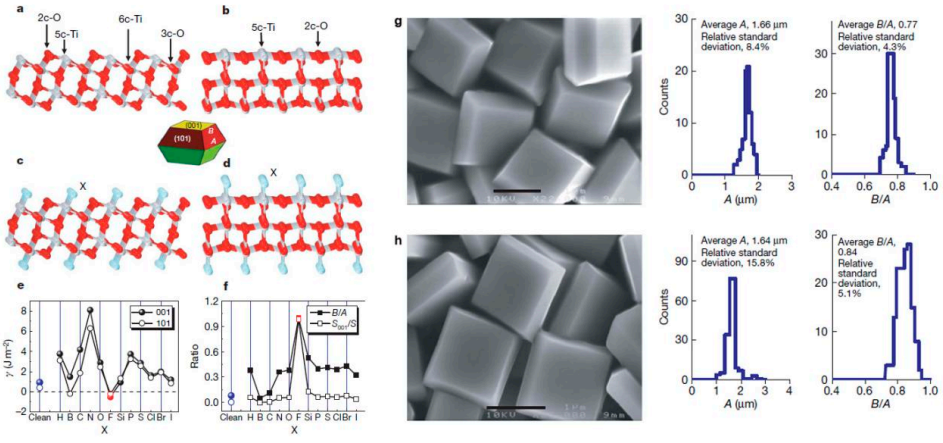

Figure 4. Theoretical calculation guides the modification of surface/interface structures. (a-f) Slab models and calculated surface energies of anatase TiO_2 (001) and (101) surfaces. (a, b) Unrelaxed, clean (001) and (101) surfaces; (c, d) Unrelaxed (001) and (101) surfaces surrounded by adsorbate X atoms; (e) Calculated energies of the (001) and (101) surfaces surrounded by X atoms; (f) Plots of the

Preprints (www.preprints.org) | NOT PEER-REVIEWED | Posted: 1 October 2017 doi:10.20944/preprints201710.0002.v1

Peer-reviewed version available at Nanomaterials 2017, 7, 382; doi:10.3390/nano7110382

optimized value of B/A and percentage of {001} facets for anatase single crystals with various adsorbate atoms X. (g, h) SEM images and statistical data for the size and truncation degree of anatase single crystals (reprinted from [28] with permission, Copyright Nature Publishing Group, 2008).

3. Applications of Surface/Interface Engineered TiO_2 Micro/Nanostructures

Surface and interface structures of TiO_2 materials play important roles in multiple physical/chemical processes. Herein, we will highlight the recent progress in the research activities on the surface/interface engineered TiO_2 micro/nanostructures used for photocatalysis (including photocatalytic degradation of organic contaminants, photocatalytic hydrogen evolution, and photocatalytic CO_2 reduction), lithium/sodium ion batteries, and Li-S batteries.

3.1. Photocatalysis

There are 4 main steps involved in heterogeneous photocatalysis process (Figure 5a): (1) light absorption; (2) the generation and separation of photoexcited electrons and holes; (3) the migration, transport and recombination of carriers; and (4) surface electrocatalytic reduction and oxidation reactions. The overall photocatalysis efficiency is strongly dependent on the cumulative effects of these four consecutive steps. Among different photocatalyst materials, TiO_2 is considered to be a remarkable photocatalyst due to the notable merits such as nontoxicity, biological compatibility, and universality. However, for practical use of pristine TiO_2 materials, the photocatalytic activity is hampered by the intrinsic limitations of the wide bandgap and the high electron-hole recombination rate. Only UV light can activate the TiO_2 photocatalysts an the UV only account for less than 5% of the full solar spectrum. The high electron-hole recombination rate results in a low quantum yield and inefficiency of photocatalytic reactions. Since the photocatalytic reaction is a surface or interface sensitive process, control of the surface/interface structures in TiO_2 materials provides a possible way to improve the light absorption and visible light usage, and facilitate the carrier separation, resulting in enhanced photocatalytic properties. Many attempts have been carried out to modify the surface or interface structures of TiO_2 materials, such as exposed crystallographic plane tuning, defect engineering, interface construction, and so on (Figure 5b-d). In the following, we will discuss the effects of 3 surface/interface modification routes on photocatalytic degradation of organic contaminants, photocatalytic hydrogen evolution, and photocatalytic CO_2 reduction.

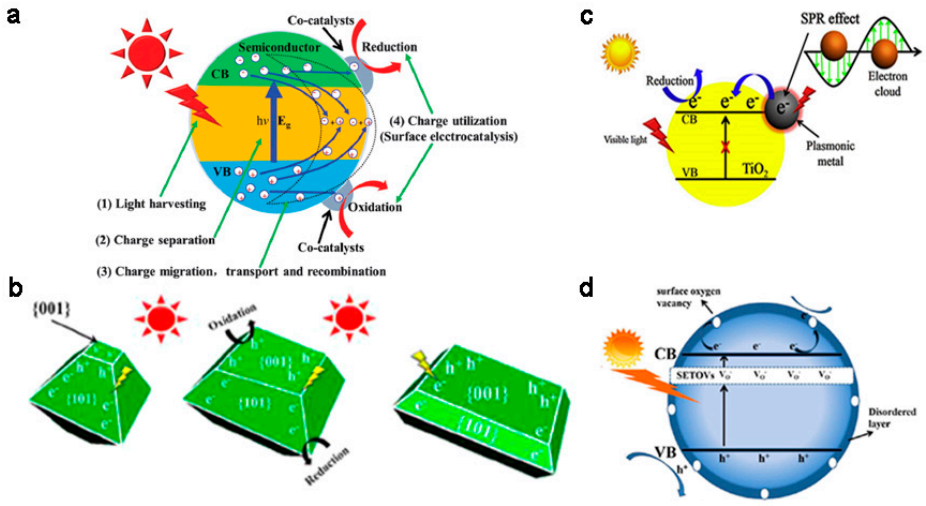

Figure 5. (a) Different stages in heterogeneous photocatalysis (reprinted from [44] with permission, The Royal Society of Chemistry, 2016); surface/interface engineered TiO_2 structures for photocatalytic improvement: (b) crystallographic plane tuning (reprinted from [45] with permission, American Chemical Society, 2014), (c) defects engineering (reprinted from [46] with permission,

Elsevier B.V., 2016), and (d) creating interfaces in TiO_2 nanostructures (reprinted from [47] with permission, Elsevier B.V., 2017).

3.1.1. Photocatalytic Degradation of Organic Contaminants

With a rapidly growing world population and expanding industrialization, development of new materials, techniques and devices those can provide safe water and air is important to the societal sustainability. Semiconductor photocatalysis has been utilized as an ideal way to degrade various organic contaminants in water and air. TiO_2 nanostructures with tailored surface and interface have been demonstrated as enhanced photocatalytic efficiency in the degradation of pollutants.

Edy *et al*. synthesized free-standing TiO_2 nanosheets with different thickness via atomic layer deposition on a dissolvable sacrificial polymer layer [48]. The photocatalytic performance was evaluated for photocatalytic degradation of methyl orange under UV light irradiation. The photocatalytic activity increases with increasing the thickness, which maybe due to the existence of Ti^{3+} defect and locally ordered domain structures in the amorphous nanosheets. TiO_2 nanostructures with exposed highly reactive facets, for example, anatase TiO_2 nanosheets with {001} facets, are desirable for the photocatalytic enhancement. Those thin nanosheets are prone to aggregate during the practical usage, which results in the loss of photocatalytic activity. Assembly the individual nanostructure into hierarchical architecture can not only suppress the aggregation of micro/nanoscale building blocks, but also increase specific surface area and the amount of active reaction sites, and reduce the diffusion barrier. We synthesized anatase TiO_2 hollow microspheres assembled with high-energy {001} facets via a facile one-pot hydrothermal method [49]. The percentage of exposed {001} facets on the microspheres was estimated to be about 60%. The photocatalytic ability was evaluated by photodegradation of methylene blue under UV light. The photocatalytic degradation reaction follows pseudo-first-order kinetics among the studied samples. The apparent photochemical degradation rate constant for the hierarchical TiO_2 structures is 4.07×10^{-2} min^{-1}, which is faster than that of control samples (P25 powders, 3.11 × 10−2 min^{-1}; porous TiO_2 powders, 2.76×10^{-2} min^{-1}; the etched TiO_2 spheres, 2.17×10^{-2} min^{-1}; the irregular TiO_2 product, 0.86×10^{-2} min^{-1}). The good photocatalytic activity of the hierarchical TiO_2 structures is associated with the hollow structures with bimodal mesopore size distribution and relatively large BET surface areas. Xiang *et al*. synthesized a kind of hierarchical flower-like TiO_2 superstructures by alcohothermal treatment method [50]. The superstructures were consisted by anatase TiO_2 nanosheets with 87% exposed (001) facets. Photocatalytic oxidative decomposition of acetone was evaluated in air under UV light. The results show that the photocatalytic activity of the flower-like TiO_2 superstructures was better than that of P25 and tubular shaped TiO_2 particles. The synergetic effect of highly exposed (001) facets hierarchically porous structure, and the increased light-harvesting capability is responsible for the enhanced photocatalytic ability.

Besides the exposed high energy facets, the introduction of suitable defect structures in TiO_2 materials can obviously influence the light absorption and the separation of photogenerated electron-hole pairs [51-53]. Cao *et al*. fabricated mesoporous black TiO_2 spheres with high crystallinity by a facile evaporation-induced self-assembly method combined with a mild calcinations after an *in-situ* hydrogenation under an argon atmosphere [51]. The results indicated the prepared sample was uniform mesoporous black spheres with Ti^{3+} and N co-doping. The visible-light-driven photocatalytic degradation ratio of methyl orange was up to 96%, which was several times higher than that of pristine TiO_2 material. The excellent photocatalytic activity was due to Ti^{3+} and N doping, which resulted in high visible light utilization and enhanced separation of photogenerated charge carriers, and the mesoporous network structures.

Generating interface structures by depositing plasmonic-metal nanostructures (Ag, Pt, Au, etc) on TiO_2 materials can increases the generation rate of energetic charge carriers and result in a higher probability of redox reactions [54-57]. By using successive ion layer adsorption and reaction, Shuang *et al*. synthesized TiO_2 nanopillar arrays with both Au and Pt nanoparticles (~ 4 nm) decoration [54]. Due to the electron-sink function of Pt and surface plasmon resonance of Au nanoparticles, the

charge separation of photoexcited TiO_2 was improved. The obtained Au/Pt nanoparticles decorated TiO_2 nanopillar arrays showed much higher visible and UV light absorption response, which leaded to remarkably enhanced photocatalytic activities the degradation of methyl orange.

3.1.2. Photocatalytic hydrogen evolution

Hydrogen energy is one of the most promising green fuels. Since the first discovery of photoelectrochemical water splitting by Fujishima and Honda in 1972, hydrogen production directly from water and sunlight on semiconductor materials has been intensively investigated [3]. Although numerous semiconductor materials have been explored as photocatalysts to produce hydrogen, TiO_2 remains one of the most studied material for photocatalytic H_2 evolution due to the main merits of nontoxic and chemical stability.

The morphology of TiO_2 nanostructures, especially those with highly reactive exposed facets, are related to the photocatalytic activity enhancement. For example, Wu *et al*. synthesized mesoporous rutile TiO_2 single crystal with wholly exposed {111} facets by a seeded-template method. Fluoride ions in the solution played an important role in stabilizing the high energy facet {111} of rutile TiO_2 [58]. The ratios of exposed {110} and {111} facets can be controlled by by tuning the concentration of fluoride ions. The mesoporous single crystal rutile TiO_2 with wholly exposed {111} reactive facets exhibited a greatly enhanced photocatalytic hydrogen generation. Zhang *et al*. demonstrated that the TiO_2 single crystal with a novel four-truncated-bipyramid morphology can be synthesized by a facile hydrothermal reaction [59]. The resultant photocatalyst exhibited excellent hydrogen evolution activity from ethanol-water solution. The exposure of both high-energy {001} oxidative and low-energy {101} reductive facets in an optimal ratio are thought to be the key factors for the high photocatalytic activity. In another example, anatase TiO_2 nanoplates with exposed (001) facet were converted from the NH_4TiOF_3 nanoplates [60]. The obtained compact TiO_2 nanoplates exhibited a high H_2-production rate of 13 $mmolh^{-1}g^{-1}$ with a H_2-production quantum efficiency of 0.93% at 365 nm.

The influence of defect structures in TiO_2 materials on photocatalytic H_2-evolution is complicated. For one thing, the defects could introduce additional states in the band gap, which cause the recombination of carriers and the weaken of carriers' oxidation and reduction capacities [61-64]. For another, subtly generating specific defects will facilitate the separating of the carriers. Recently, Wu *et al*. prepared yellow TiO_2 nanoparticles with ultra-small size of ~3 nm [61]. Simulated solar light driven catalytic experiments showed that the evolved H_2 for the yellow TiO_2 was ~48.4 $\mu molh^{-1}g^{-1}$, which was ~3.7 fold comparing to that of the normal TiO_2 (~13.1 $\mu molh^{-1}g^{-1}$) at the same experimental conditions. It is suggested that the significantly improved H_2-evolution activity can be attributed to the coexistence of titanium vacancies (acceptor) and titanium interstitials (donor) in the TiO_2 materials, which is beneficial for the spontaneous separation of photo-generated charge-carriers. Compared to the complex steps that are required to accurately control of the defects, passivation of the defect states with elemental doping would be more direct. Recent works show that Mg doping could eliminate the intrinsic deep defect states and weaken the shallow defect states in TiO_2 materials [64]. The result was confirmed by the transient infrared absorption-excitation energy scanning spectroscopic measurement. The photocatalytic over-all water splitting measurements showed the H_2 and O_2 evolution rates can be as high as 850 and 425 $molh^{-1}g^{-1}$ under AM 1.5 G irradiation and the apparent quantum efficiency of 19.4% was achieved under 350 nm light irradiation.

Rational creating hetero- or homo-interfaces in TiO_2 materials is an efficient strategy to separate photogenerated carriers, improve visible and near-infrared photo-absorption, and thus achieve high-performance photocatalytic hydrogen evolution. Compared to the pure crystalline and amorphous TiO_2 film, high electron concentration and mobility can be concurrently obtained at the homo-interface between crystalline and amorphous layers in a bilayer TiO_2 thin film. Therefore, extraordinary properties could be explored in well-designed interfaces with homogeneous chemical composition. By creating a crystalline Ti^{3+} core/amorphous Ti^{4+} shell structure, Yang *et al*. successfully activated rutile TiO_2 material with efficient photocatalytic hydrogen evolution

properties [65]. The average hydrogen evolution rate was enhanced from 1.7 for pure TiO_2 to 268.3 $\mu molh^{-1}$ for TiO_2 with homointerface structures. The origin of the activation was attributed to the regulated the transport behaviors of holes and electrons from the bulk of a particle to the surface by suppressing the transport of electrons in the conduction band and facilitating the transport of holes in the valence band. In addition, hetero-interfaces between TiO_2 materials and other semiconductor or metal nanostructures, including carbon, Si, NiO, ZnS, CdS, MoS_2, MoC_2, layered double hydroxides, and plasmonic metals, has been extensively investigated [66-72]. As an example, Wu *et al*. reported that anisotropic TiO_2 overgrowth on Au nanorods can be obtained by selective spatial assembly and subsequent hydrolysis [66]. Plasmon-enhanced H_2 evolution under visible/near-infrared light irradiation has been demonstrated. The Au nanorod-TiO_2 interface with the Au nanorod sida exposed, as a Schottky junction, can filter out surface plasmon resonance hot electrons from the Au nanorod, which is crucial to boosting the H_2 evolution performance.

3.1.3. Photocatalytic CO_2 Reduction

Due to the increasing consumption of conventional fossil fuels, the concentration of greenhouse gas, especially CO_2, steadily grows over years. Solar-light-driven reduction of CO_2 to useful chemical fuels (such as CH_4, HCO_2H, CH_2O, and CH_3OH) is a promising solution for the serious environmental and energy problems. In the process of photocatalytic CO_2 reduction, typical steps including adsorption of CO_2, generation of electron-hole pair, separation and migration of electron-hole pair, and the reduction of CO_2 are involved. Since CO_2 molecules are highly stable, only the electrons with sufficient reduction potential can be utilized to trigger CO_2 reduction reactions, and suitable photocatalyst is required to decrease the high reaction barrier. Among a wide range of metal and semiconductor photocatalysts for CO_2 reduction, TiO_2 materials has attracted much attention due to the advantageous of high reduction potential, low cost and high stability. The activity, selectivity, and durability of TiO_2 photocatalysts for CO_2 reduction is related to the efficiency of electron-hole separation and light utilization ability, which are very sensitive to the surface structure, atomic configuration and chemical composition of the photocatalysts. For example, metal or non-metal doping is an effective method to narrow the bandgap of TiO_2 materials, which results in an extension of light absorption range from UV into visible light range. The doping of metal elements induces the substitution of titanium atoms and creating empty energy level below the conduction band, while the doping of non-metal elements by replacing the oxygen atoms in the TiO_2 lattice yields additional energy level above the valance band. Different kinds of metals (transition, rare, alkali earth metals) have been studied as doping to improve the photocatalytic activity for CO_2 reduction [73-75]. Compared to the metal doping method, which usually suffers from photocorrosion problem, non-metal (carbon, nitrogen, iodine, sulfur, etc) doping has attracted more attention [76]. However, a large amount of non-intrinsic defects often generated during the doping and created electron-hole recombination centers at the same time. Herein, we mainly focus on surface/interface modification to enhance the performance of TiO_2 photocatalysts towards CO_2 reduction.

Yu *et al*. investigated the effect of different exposed facets of anatase TiO_2 crystals on the photocatalytic CO_2 reduction activity [45]. By using a simple fluorine-assisted hydrothermal method, they synthesized anatase TiO_2 with different ratios of the exposed {101} and {001} facets. The results showed that the photocatalytic activity of the anatase TiO_2 with the optimized ratio of exposed {001} to {101} facet (55:45) was ~4 times higher than that of P25 powder. They ascribed the enhancement to a concept of 'surface heterojunction', which driven electron and hole to the {101} and {001} facets (the electron-hole separation) based on the band alignment. It is worth mentioning that surface atomic and defect structures on different facets should also contribute the photocatalytic CO_2 reduction processes. Truong *et al*. synthesized rutile TiO_2 nanocrystals with exposed high-index facets through solvothermal reaction by using a water-soluble titanium-glycolate complex as a precursor [77]. Structural characterizations showed that each branched nanocrystal was bound by 4 facets of high-index {331} facets, and rutile {101} twinned structures were formed in the boundary of branches.

The photocatalytic CO_2 reduction to methanol showed a significantly higher activity was achieved in the synthesized nanostructures due to the abundant surface defects on the high energy facts.

Generating oxygen vacancies is effective to modulate the electronic/optical properties and thus optimize diverse applications of metal oxides. Generally, bulk oxygen vacancies formed a middle sub-band in the forbidden gap, which made TiO_2 response to the visible light, and those bulk oxygen vacancies also acted as the electron-hole recombination centers. The surface oxygen vacancies not only showed a strong response to the visible light, but also acted as the capture traps to inhibit electrons-holes recombination. By adjusting the the concentration ratio of the surface and bulk oxygen vacancies, it is possible to improve the photocatalytic efficiency of TiO_2 nanostructures. Li *et al.* compared the effects of oxygen vacancies in TiO_2 nanocrystals on the photoreduction of CO_2 [47]. By choosing the precursors and post-treatment conditions, they obtained three kinds of TiO_2 materials with different oxygen vacancies, i.e., TiO_2 with surface oxygen vacancies (TiO_2-SO), TiO_2 with bulk single-electron-trapped oxygen vacancies (TiO_2-BO), and TiO_2 with mixed vacancies (TiO_2-SBO). By analyzing the lifetime and intensity by positron annihilation, the efficiency of photocatalytic CO_2 reduction improved with the increase of the ratio of surface oxygen vacancies to bulk ones. The results revealed the critical role of surface/bulk defects in photocatalytic properties.

Similar with the case of photocatalytic hydrogen evolution, creating metal- or semiconductor-TiO_2 interface via different post-deposition or *in-situ* forming methods has been demonstrated to be effective to improve the light harvesting and the separation of charged carriers, which are also important for the photoreduction of CO_2. Specifically, Schottky barrier can be formed when the Fermi level of the deposited metals are lower than the conductor band of the TiO_2 materials, which is favorable for the spatial separation of electron-hole pairs. Platinum, which possesses suitable work function, is one of the most commonly used metal co-catalyst to improve the CO_2 reduction performance of TiO_2 photocatalysts. However, worldwide limited source and consequent high price of platinum seriously hinder the large scale applications. The deposition of plasmonic nanostructures of metals such as silver and gold on TiO_2 materials has been extensively studied due to the surface plasmon resonance (SPR) effect, which shows important role in improving the photocatalytic activity for CO_2 reduction.

3.2. Lithium/Sodium Ion Batteries

Rechargeable lithium ion battery is one of the most important energy storage devices for portable electronics and hybrid/electric vehicles. The overall performance of lithium ion batteries is highly dependent on the inherent properties of the electrode materials. Among many potential electrode candidates, titanium dioxides with typical phase structures (anatase, rutile, brookite, TiO_2(B)) have attracted much attention due to the abundance of raw materials and environmental benignity. Although the theoretical specific capacity of titanium dioxides (335 $mAhg^{-1}$, according to the electrochemical reaction $TiO_2 + xLi + xe \leftrightarrow Li_xTiO_2$ with the maximum insertion coefficient x determined to be ~0.96) is comparable to that of commercial graphite (372 $mAhg^{-1}$), these materials possess a higher operating voltage platform than that of graphite, which is favorable for inhibiting the formation of lithium dendrite and solid-electrolyte interphase (SEI) layer. Moreover, the minor volume variation during cycling ensures a good cycling stability. It should be noted that the intrinsic poor electronic conductivity and sluggish lithium ion diffusion limit the high-rate performance of these materials. The size, shape, composition, and assembly of TiO_2 anodes are intensively investigated to optimize the lithium storage properties.

Recent works also show that nanoscale surface/interface design in TiO_2 nanostructures is beneficial for improving energy density, capacity retention, and rate capability (Table 1), which are ascribed to the large surface area, numerous active sites, short mass and charge diffusion distance, and efficient accommodation of volume changes during charging and discharging process. For example, theoretical and experimental results demonstrated that lithium insertion was favored on the high-energy {001} surface of anatase TiO_2, which has a more open structure and short path for lithium ion diffusion along this direction. Since the important breakthrough in preparation of anatase TiO_2 single crystals with exposed {001} facets achieved by Yang *et al.*, extensive studies have been

reported on the synthesis of TiO_2 anodes with exposed {001} facets [78]. However, most of these anatase TiO_2 are crystals with two-dimensional sheetlike, which make the sheets easily over-lap with each other to reduce the overall surface energy. Preventing the aggregation of these crystals with large amount of exposed {001} facets is a big challenge. By using a simple one-pot solution method, we successfully obtained 3D anatase TiO_2 hollow microspheres assembled with high-energy {001} facets (Figure 6a) [79]. In the synthesis, a mixture containing Ti powder, deionization water, hydrogen peroxide, and hydrofluoric acid was subjected to hydrothermal treatment at 180 °C. The addition of hydrofluoric acid and hydrogen peroxide is critical for the formation of {001} facet assembly. The Bruauer–Emmett–Teller (BET) specific surface area of the product is ca. 43.3 $m^2 g^{-1}$. The isotherm corresponding to the product is of type IV with two capillary condensation steps, implying bimodal pore size distributions in the mesoporous and macroporous regions. The as-prepared sample shows good cyclic capacity retention during cycling. A reversible capacity of 157 $mAhg^{-1}$ can be retained after 50 cycles with about 75% retention as compared with the first reversible capacity. Rate performance test show that after the first 10 cycles at the rate of 1 C (1 C = 335 $mAhg^{-1}$), the discharge capacity reaches about 156 $mAhg^{-1}$, and then it slightly reduces to 135 and 130 $mAhg^{-1}$ at rates of 2 and 5 C, respectively. Even for a rate as high as 10 C, the electrode can deliver a reversible capacity of 90 $mAhg^{-1}$. When the current rate is returned to the initial value of 1 C, the electrode resumes its original capacity of about 150 $mAhg^{-1}$ after 10 cycles.

Although rutile phase is most thermodynamically stable which can easily be obtained at higher temperatures, bulk rutile TiO_2 is demonstrated to be unfavorable for the intercalation of Li ions. Comparing to its bulk counterpart, nanoscale rutile TiO_2 particles show a much higher electroactivity towards lithium insertion at room temperature. However, the particle aggregation associated with the Li insertion and extraction processes are common problems during the practical use of rutile TiO_2 in lithium ion batteries. Unsatisfactory electrochemical performance caused by kinetic limitations also impedes its applications. To improve the lithium storage properties of rutile TiO_2 anodes, the synthesis of nanostructured materials with suitable surface/interface configurations and improved conductivity has been shown to be an effective approach to overcome the above limitations. We synthesized rutile TiO_2 nanoparticles by a facile solution and subsequent thermal annealing method (Figure 6b) [35]. Each particle surface was etched to form pits with average size of 2–5 nm (quantum pits). Compared to the nanoparticles with other morphology, the obtained rutile TiO_2 nanoparticles with quantum pits (QP-TiO_2 NPs) possessed more unsaturated bond and other defect structures, such as terraces, steps, and kinks, which provided more active sites for lithium ions storage and enhance the conductivity. As a consequence, the yielded QP-TiO_2 NPs exhibited a maximum specific capacity of 145$mAhg^{-1}$ at a current density of 0.5 C with outstanding charge/discharge rate capability (102 $mAhg^{-1}$ at 5 C) and good cycling performance, demonstrating a great potential as anode materials for lithium ion battery applications.

Table 1. Performance comparison of some lithium ion batteries and sodium ion batteries based on typical TiO_2 anodes (the voltage is versus Li^+/Li or Na^+/Na).

Material/[Ref.]	Capacity (cycles) ($mAhg^{-1}$)	Rate capability ($mAhg^{-1}$)	Voltage (V)
TiO_2 Microboxes [80]	187 (300)@170 mAg^{-1}	63@3400 mAg^{-1}	1-3/Li
Rutile TiO_2 inverse opals [81]	95 (5000)@450 mAg^{-1}	-	1-3/Li
Faceted TiO_2 Crystals [82]	141.2 (100)@170 mAg^{-1}	29.9@1700 mAg^{-1}	1-3/Li
Nanosheet-Constructed TiO_2–B [83]	200 (200)@3350 mAg^{-1}	216@3350 mAg^{-1}	1-3/Li
TiO_2 hollow microspheres [79]	157 (50)@170 mAg^{-1}	90@1700 mAg^{-1}	1-3/Li
rutile TiO_2 nanostructures [84]	190 (200)@102 mAg^{-1}	84.5@1700 mAg^{-1}	1-3/Li
nest-like TiO_2 hollow microspheres [85]	152 (100)@1020 mAg^{-1}	130@3400 mAg^{-1}	1-3/Li
Co_3O_4 NPs@TiO_2(B) NSs [86]	677.3 (80)@100 mAg^{-1}	386@1000 mAg^{-1}	0.01-3.0/Li
TiO_2-B@VS_2 nanowire arrays [87]	365.4 (500)@335 mAg^{-1}	171.2@3350 mAg^{-1}	0.01-3.0/Li

Preprints (www.preprints.org) | NOT PEER-REVIEWED | Posted: 1 October 2017 doi:10.20944/preprints201710.0002.v1

Peer-reviewed version available at Nanomaterials 2017, 7, 382; doi:10.3390/nano7110382

Nb-Doped Rutile TiO_2 Mesocrystals [88]	141.9 (600)@850 mAg^{-1}	96.3@6800 mAg^{-1}	1-3/Li
TiO_2@defect-rich MoS_2 nanosheets [89]	805.3 (100)@100 mAg^{-1}	507.6@2000 mAg^{-1}	0.005-3.0/Li
MoS_2-TiO_2 based composites [90]	648 (400)@1000 mAg^{-1}	511@2000 mAg^{-1}	0.005-3.0/Li
macroporous TiO_2 [91]	181 (1000)@1700 mAg^{-1}	69@12.5 Ag^{-1}	1-3/Li
porous TiO_2 hollow microspheres [92]	216 (100)@170 mAg^{-1}	112@1700 mAg^{-1}	1-3/Li
porous TiO_2(B) nanosheets [93]	186 (1000)@1675 mAg^{-1}	159@6700 mAg^{-1}	1-3/Li
graphene supported TiO_2(B) sheets [94]	325 (10000)@500 mAg^{-1}	49@40 Ag^{-1}	1-3/Li
mesoporous TiO_2 coating on carbon [95]	210 (1000)@3400 mAg^{-1}	150@10.2 Ag^{-1}	1-3/Li
Ti^{3+}-free three-phase $Li_4Ti_5O_{12}$/TiO_2 [96]	136 (1000)@4000 mAg^{-1}	155.6@8 Ag^{-1}	1.0-2.5/Li
TiO_2-Sn@carbon nanofibers [97]	413 (400)@100 mAg^{-1}	-	0.01-2.0/Na
Double-walled Sb@TiO_{2-x} nanotubes [98]	300 (1000)@2.64 Ag^{-1}	312@13.2 Ag^{-1}	0.1-2.5/Na
Carbon-coated anatase TiO_2 [99]	180 (500)@1675 mAg^{-1}	134@3.35 Ag^{-1}	0.05-2.0/Na
Nanotube arrays of S-doped TiO_2 [100]	136 (4400)@3350 mAg^{-1}	167@3350 mAg^{-1}	0.1-2.5/Na
Amorphous TiO_2 inverse opal [101]	203 (100)@100 mAg^{-1}	113@5 Ag^{-1}	0.01-3.0/Na
Petal-like rutile TiO_2 [102]	144.4 (1100)@837.5 mAg^{-1}	59.8@4187 mAg^{-1}	0.01-3.0/Na
Yolk-like TiO_2 [103]	200.7 (550)@335 mAg^{-1}	90.6@8375 mAg^{-1}	0.01-3.0/Na

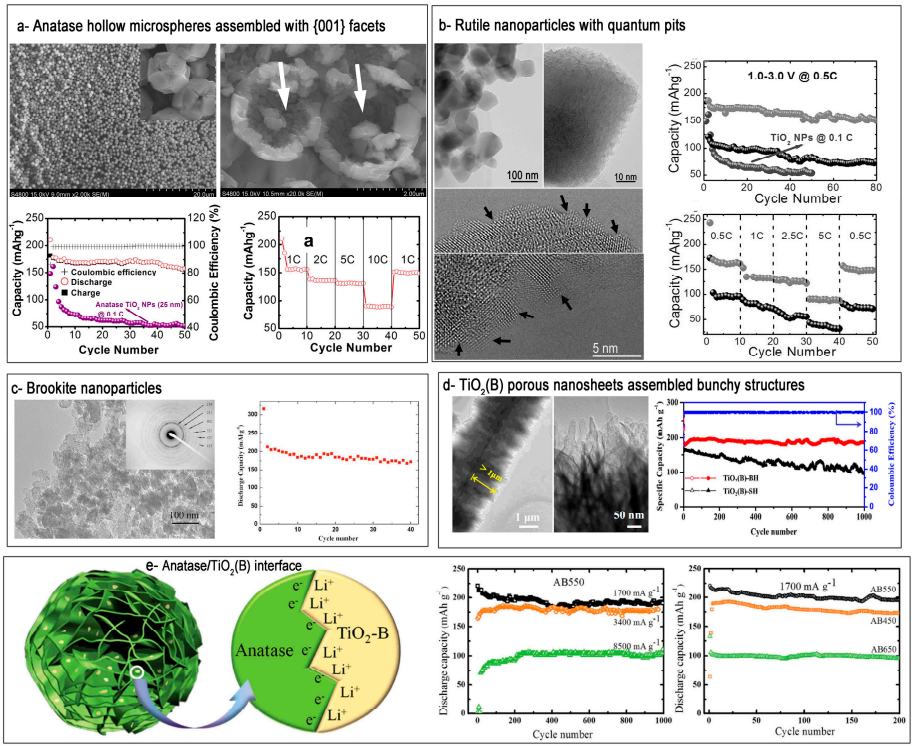

Figure 6. Typical TiO_2 anodes and their lithium storage properties: (a) 3D anatase TiO_2 hollow microspheres assembled with high-energy {001} facets (reprinted from [79] with permission, Copyright The Royal Society of Chemistry, 2012); (b) Rutile TiO_2 nanoparticles with quantum pits (reprinted from [35] with permission, Copyright The Royal Society of Chemistry, 2016); (c) Brookite TiO_2 nanocrystalline (reprinted from [105] with permission, Copyright The Electrochemical Society, 2007); (d) bunchy hierarchical TiO_2(B) structure assembled by porous nanosheets (reprinted from [93] with permission, Copyright Elsevier Ltd., 2017); (e) Ultrathin anatase TiO_2 nanosheets embedded with TiO_2(B) nanodomains (reprinted from [107] with permission, Copyright John Wiley & Sons, 2015).

Among the different TiO_2 polymorphs investigated, a severe capacity fading was noted for the brookite phase, although it exhibited nearly one mole of reversible lithium insertion/extraction in its nanostructured form [104]. There has not been extensive research focused on developing such an anode. Reddy *et al.* demonstrated intercalation of lithium into brookite TiO_2 nanoparticles (Figure 6c). Electrochemical test and *ex-situ* XRD studies showed that the structure was stable for lithium intercalation and deintercalation although the intercalation/deintercalation mechanism was not clear. Cycling performance of brookite TiO_2 performed at C/10 rate in the voltage window 1.0–3.0 V showed that the capacity was gradual loss during initial 10 cycles and the capacity is fairly stable at 170 $mAhg^{-1}$ on further cycling. In contrast to other TiO_2 polymorphs, TiO_2(B) phase possesses relatively more open crystal structure, which allows the facile insertion/extraction of lithium ions. Moreover, a lower operating potential (~ 1.55 V vs. Li) compared to the anatase TiO_2 (~ 1.75 V vs. Li), an improved reversibility, and a high rate capability make TiO_2(B) phase a promising candidate for lithium storage. Li *et al.* reported on the orderly integration of porous TiO_2(B) nanosheets into bunchy hierarchical structure (TiO_2(B)-BH) via a facile solvothermal process (Figure 6d). Benefiting from the unique structural merits, TiO_2(B)-BH exhibited high reversible capacity, long-term cycling stability (186.6 $mAhg^{-1}$ at 1675 mAg^{-1} after 1000 cycles) and desirable rate performance.

Recently, Jamnik and Maier proposed that it was possible to storage additional lithium at the interface of nanosized electrodes, which included solid–liquid (electrode-electrolyte) interface and solid–solid interface between the electrodes (Figure 6e) [106,107]. The interfaces can accommodate additional Li ions, leading to a rise of total Li storage. Meanwhile, an additional synergistic storage is favored if the electrode material is made of a lithium ion-accepting phase and an electron-accepting phase which is benefit for charge separation ("Job-sharing" mechanism). Along this line, Wu *et al*. synthesized a new kind of microsphere constructed by ultrathin anatase nanosheets embedded with TiO_2(B) nanodomains, which contained a large amount of interfaces between the two phases [107]. The hierarchical nanostructures show capacities of 180 and 110 $mAhg^{-1}$ after 1000 cycles at current densities of 3400 and 8500 mAg^{-1}. The ultrathin nanosheet structure which provides short lithium diffusion length and high electrode/electrolyte contact area also accounts for the high capacity and long-cycle stability. This study highlights the importance of smart design the interface structures in the nanoelectrodes.

Although the development and commercialization of lithium ion batteries have achieved great success in the past years, one severe drawback of lithium ion batteries is the limited lithium resource in the Earth's crust and its uneven geographical distribution. In this regard, sodium ion batteries have attracted particular attention due to the obvious advantageous including high earth-abundance of sodium, and lower cost vs. lithium ion batteries. In addition, the sodium chemistry is similar as the case of lithium, so the previously established surface/interface engineering strategies for titanium dioxides electrode design in lithium ion batteries system can be transferred to and expedite the odium ion battery studies. Longoni *et al*. systematically studied the role of different exposed crystal facets of the anatase nanocrystals on the sodium storage properties [24]. By employing a surfactant-assisted solvothermal route, they synthesized anatase TiO_2 nanostructures with three different morphologies (Rhombic elongated (RE), rhombic (R), and nanobar (NB)), which showed obvious differences in crystal face type exposition. Their electrochemical performance results together with theoretical analysis showed that an overcoordinated state of Ti atoms on the crystal surface (low energy density (101) facets of NB and R moieties) strongly inhibits the sodium uptake, while a Goldilocks condition seems to occur for crystalline faces with intermediate energy densities, like (100) in RE. Zhang *et al*. reported a smart design of the assembly and interface of rutile TiO_2 and fewer layer graphene by using carbon dots as designer additives [102]. The resultant graphene-rich petal-like rutile TiO_2 showed outstanding sodium-storage properties. At a rate of 0.25 C (83.75 mAg^{-1}) after 300 cycles, a high capacity of 245.3 $mAhg^{-1}$ was achieved, even at a high current density of 12.5 C (4187.5 mAg^{-1}), a considerable capacity of 59.8 $mAhg^{-1}$ can still be maintained. Notably, the reversible capacity up to 1100 cycles at a current density of 2.5 C (837.5 mAg^{-1}) can still reach 144.4 $mAhg^{-1}$; even after 4000 cycles at 10 C (3350 mAg^{-1}), a capacity retention of as high as 94.4% is obtained. Zhang *et al*. demonstrated the positive function of oxygen vacancies in TiO_2(B) nanobelts

Preprints (www.preprints.org) | NOT PEER-REVIEWED | Posted: 1 October 2017 doi:10.20944/preprints201710.0002.v1

Peer-reviewed version available at Nanomaterials 2017, 7, 382; doi:10.3390/nano7110382

for the enhancement of sodium storage [108]. The sample displayed the significantly superior sodium-storage properties, including a higher capacity (0.5 C; 210.5 $mAhg^{-1}$ vs 102.7 $mAhg^{-1}$), better rate performance (15 C; 89.8 vs 36.7 $mAhg^{-1}$), compared to those of pristine TiO_2(B) electrodes without oxygen vacancies.

3.3. Li-S Batteries

Li-S batteries possess exceptionally high theoretical energy densities ~2600 $Wh{\cdot}kg^{-1}$ vs. 580 $Wh{\cdot}kg^{-1}$ of today's best batteries. Li-S batteries contain low cost materials, sulfur is highly abundant, and the anode consists of lithium metal and does not limit the capacity. Today's Li-S technology fails short in energy density and lifetime because of the limited sulfur loading that can be achieved in the cathode, due to the poor conductivity of sulfur deposits, because of the solvation into the electrolyte of the discharge products (i.e. Li_xS_y polysulfides), and finally because of the large volume expansion of sulfur during the battery cycling affecting the cathode integrity.

Cathodes with high surface area and high electronic conductivity are crucial to improve sulfur loading and rate performance of Li-S batteries. The polysulfides "shuttle" phenomena, via the solvation of the polysulfides in the electrolyte, gradually decreases the mass of active material, leading to continuous fading in capacity and must be avoided. Therefore, the candidate cathodes should have porous and conductive nature as well as suitable interactions with polysulfides simultaneously. To overcome those obstacles, a wide range of strategies have been developed, including encapsulation or coating of the sulfur electrode, use of impermeable membranes, and/or use of electrolytes that minimize the solubility and diffusivity of the polysulfides. However, none of these solutions has led to acceptable results, fulfilling all the requirements. For example, the main disadvantage of widely used porous conductive carbon electrodes lies in weak physical confinement of lithium sulfides, which is insufficient to prevent the diffusion and shuttling of polysulfides during long-term cycling. Therefore, ideal electrodes should not only possess porous and conductive nature, but also suitable interactions with polysulfides.

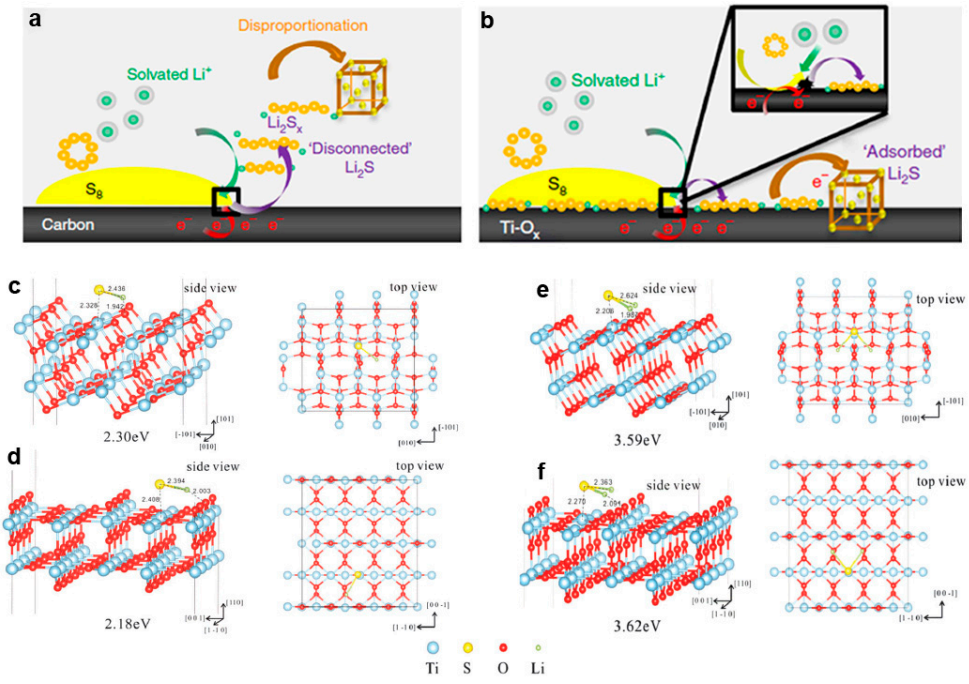

Figure 7. The interaction between sulfur or lithium polysulphides and electrodes. (a) On reduction of S_8 on a carbon host, Li_2S_x desorb from the surface and undergo solution-mediated reactions leading to broadly distributed precipitation of Li_2S; (b) On reduction of S8 on the metallic polar Ti_4O_7, Li_2S_x adsorb on the surface and are reduced to Li_2S via surface-mediated reduction at the interface (reprinted from [109] with permission, Copyright Nature Publishing Group, 2014); Adsorption configuration of (c, d) Li-S* and (e, f) Li_2S on the (c, e) anatase-TiO_2 (101) surface and (d,

Preprints (www.preprints.org) | NOT PEER-REVIEWED | Posted: 1 October 2017 doi:10.20944/preprints201710.0002.v1

Peer-reviewed version available at Nanomaterials 2017, 7, 382; doi:10.3390/nano7110382

f) rutile-TiO_2 (110) surface (reprinted from [110] with permission, Copyright The Royal Society of Chemistry, 2016).

On a typical carbon support (Figure 7a), elemental sulfur undergoes reduction to form lithium polysulphides that then dissolve into the electrolyte. In the presence of a polar metal oxide as witnessed for titanium oxides, however, the solvation of the polysulfides is significantly affected (Figure 7b). Not only is the concentration of polysulphides in solution that greatly diminished during discharge but also a slow, controlled deposition of Li_2S is observed. The results are ascribed to the interface-mediated, spatially controlled reduction of the polysulphides. Yu *et al.* studied the interactions between intermediate polysulphides, final discharge product Li_2S and stable TiO_2 surface (anatase-TiO_2 (101), rutile-TiO_2 (110)) via theoretical simulation (Figure 7c-f). Their results show that the binding strength of the polysulphides to the anatase-TiO_2 (101) surface (2.30 eV) is a little higher than to rutile-TiO_2 (110) surface (2.18 eV), and the binding energy of Li_2S to the anatase-TiO_2 (101) surface (3.59 eV) is almost the same as with the rutile-TiO_2 (110) surface (3.62 eV). The values are larger than the adsorption binding energies for Li-S composites on graphene (< 1 eV), highlighting the efficacy of TiO_2 in binding with polysulfide anions via polar–polar interactions.

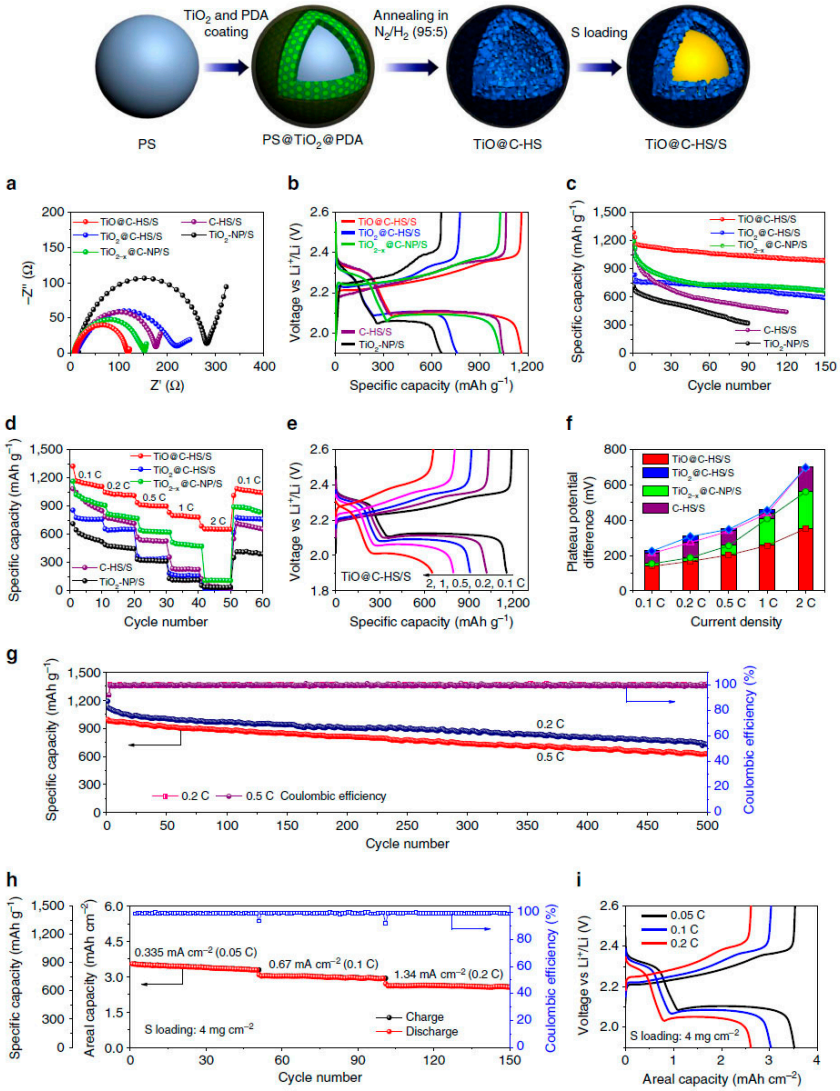

Figure 8. Schematic illustration of the synthesis process and electrochemical properties of TiO@C-HS/S composites. (a) Nyquist plots before cycling from 1 MHz to 100 mHz, (b) the second-cycle galvanostatic charge/discharge voltage profiles at 0.1 C, (c) cycle performances at 0.1 C, (d) rate capabilities and (f) the potential differences between the charge and discharge plateaus at various current densities of the TiO@C-HS/S, TiO_2@C-HS/S, TiO_{2-x}@C-NP/S, C-HS/S and TiO_2-NP/S

electrodes. (e) Voltage profiles at various current densities from 0.1 to 2 C and (g) prolonged cycle life and Coulombic efficiency at 0.2 and 0.5C of the TiO@C-HS/S electrode. (h) Areal capacities and (i) voltage profiles at various current densities from 0.335 (0.05 C) to 1.34 $mAcm^{-2}$ (0.2 C) of the TiO@C-HS/S electrode with high sulfur mass loading of 4.0 $mgcm^{-2}$ (reprinted from [25] with permission, Copyright Nature Publishing Group, 2016).

Experimentally, Cui *et al*. designed an unique sulfur-TiO_2 yolk-shell nanoarchitecture as a sulfur cathode, and achieved an initial specific capacity of 1030 $mAhg^{-1}$ at 0.5 C (1 C=1673 mAg^{-1}) and Coulombic efficiency of 98.4% over 1000 cycles [111]. Impressively, the capacity decay at the end of 1,000 cycles is found to be as small as 0.033% per cycle (3.3% per 100 cycles). The excellent properties were ascribed to the yolk–shell morphology which accommodates the large volumetric expansion of sulfur during cycling, thus preserves the structural integrity of the shell to minimize polysulphide dissolution. Based on the knowledge of chemical interactions between polysulphides and titanium oxides, a wide range of methods have been performed to optimize configuration of sulfur-titanium oxide cathodes. Typical examples include design and synthesis of porous titanium oxides high-surface area, crystalline facts engineering, conductivity enhancement by adding conductive agents (such as carbon fibers, graphene, conductive polymers) into the titanium oxide nanostructures or through annealing in inert/H_2 atmosphere. In this regard, Lou *et al.* synthesized a sulfur host containing titanium monoxide@carbon hollow nanospheres (TiO@C/S), which possess the key structural elements (i.e., high surface area, conductive, interactions with polysulfides) required for high-performance cathodes simultaneously (Figure 8) [25]. The TiO@C/S composite cathode delivered high discharge capacities of 41100 $mAhg^{-1}$ at 0.1 C, and exhibited stable cycle life up to 500 cycles at 0.2 and 0.5 C with a small capacity decay rate of 0.08% per cycle. The Li-S batteries performance based on typical titanium oxides are summarized in Table 2.

Table 2. Comparison of Li-S batteries performance based on typical titanium oxides electrode (the voltage is versus Li^+/Li).

Material/[Ref.]	Capacity (cycles) ($mAhg^{-1}$)	Rate capability ($mAhg^{-1}$)	Sulfur loading (%)	Voltage (V)
TiO_2-porous carbon nanofibers [112]	618 (500)@1675 mAg^{-1}	668 @8.375 Ag^{-1}	55	1.7-2.6
TiO_2-carbon nanofibers [113]	694 (500)@1675 mAg^{-1}	540 @3.35 mAg^{-1}	68.83	1.7-2.8
TiO_2/graphene [114]	630 (1000)@3350 mAg^{-1}	535 @5.025 Ag^{-1}	51.2	1.6-2.8
TiO_2/N-doped graphene [110]	918 (500)@1675 mAg^{-1}	833 @6.7 Ag^{-1}	59	1.7-2.8
Porous Ti_4O_7 particles [115]	989 (300)@167.5 mAg^{-1}	873 @1.675 Ag^{-1}	50-55	1.8-3.0
TiO@carbon [25]	750 (500)@335 mAg^{-1}	655 @3.35 Ag^{-1}	~70	1.9-2.6
S–TiO_2 yolk–shell [111]	1030 (1000)@837 mAg^{-1}	630 @3.35 Ag^{-1}	62	1.7-2.6
Polypyrrole/TiO_2 nanotube arrays [116]	1150 (100)@167.5 mAg^{-1}	-	61.93	1.8-3.0
Graphene-TiO_2 NPs [117]	663 (100)@1675 mAg^{-1}	-	75	1.7-2.8
TiO_2 nanowire/graphene [118]	1053 (200)@335 mAg^{-1}	-	60	1.5-2.8
graphene/TiO_2/S [119]	597 (100)@1675 mAg^{-1}	-	60	1.5-3.0
Ti_4O_7/S [109]	1070 (500)@3350 mAg^{-1}	-	70	1.8-3.0

4. Phase Stability of TiO_2 Nanostructures

As a kind of chemically stable and environmentally compatible metal oxides, TiO_2 nanostructures show fantastic physical/chemical properties and find many practical applications ranging from energy conversion and storage as mentioned above and others. The properties and applications are determined by the structures of TiO_2 materials, which is related to the external

(temperature, pressure, environment, etc) and internal (composition, stain, etc) factors. Overall, the relative phase stability in ambient bulk form is TiO_2(B) < anatase < brookite < rutile, and the specific phase shows its unique applications. For example, anatase has been found to be the most active phase in photocatalysis. TiO_2(B) phase is more favorable for the insertion/extraction of lithium ions due to the more open crystal structure compared to the other TiO_2 phases. Therefore, it is of importance to understand the phase transformation on nanoscale and improve the phase stability of the related TiO_2 nanostructures. General thermodynamic investigation, computational methods (including molecular dynamics simulations and DFT calculations), experimental routes (XRD, calorimetry, electrochemical measurements, etc.) have been successfully employed to study the phase stability and coarsening kinetics of the typical TiO_2 phases under different environment (dry, wet, hydrothermal conditions) [120]. Several excellent reviews describing the topics are available elsewhere, and we do not discuss in this paper.

With the decreasing of the size or dimension, surface and/or interface will dominate in the nanostructure and play an important role in phase stability. Due to the nature of coordination unsaturation, the atoms at the surface are more active than those within the interior. Therefore, surfaces usually exhibit a lower stability relative to the lattice interior part. For example, the melting point of free-standing nanoarticles is remarkably depressed relative to that of bulk phase (T_0). Stabilizing the surface atoms would be a way to improve the relative phase stability. Typically, when nanoparticles are properly coated by or embedded in a matrix with higher melting point, the melting point of the particles can be elevated above T_0. Herein, we focus on the strategies of surface/interface engineering to tune the phase stability in typical TiO_2 nanostructures.

We systematically studied the crystallization and structural transformation from anatase to rutile phase in the initial amorphous TiO_2 nanowires embedded in anodic aluminum oxide with different diameters (20, 50, and 80 nm, termed as TiO_2-20, TiO_2-50, and TiO_2-80 hereafter) [16]. Electron microscopy analysis and XRD results showed that the crystallization of TiO_2-20, TiO_2-50, and TiO_2-80 from amorphous to anatase occurred at ~600 °C, ~500 °C and ~400 °C, and the transformation from anatase to rutile phase started at ~900 °C, ~800 °C and ~750 °C (Figure 9). The results revealed a strong size dependence of the thermal stability of TiO_2 nanowires embedded the template. Control experiments on amorphous TiO_2 powder showed the crystallization and phase transformation temperatures were ~200 °C and ~600 °C, respectively.

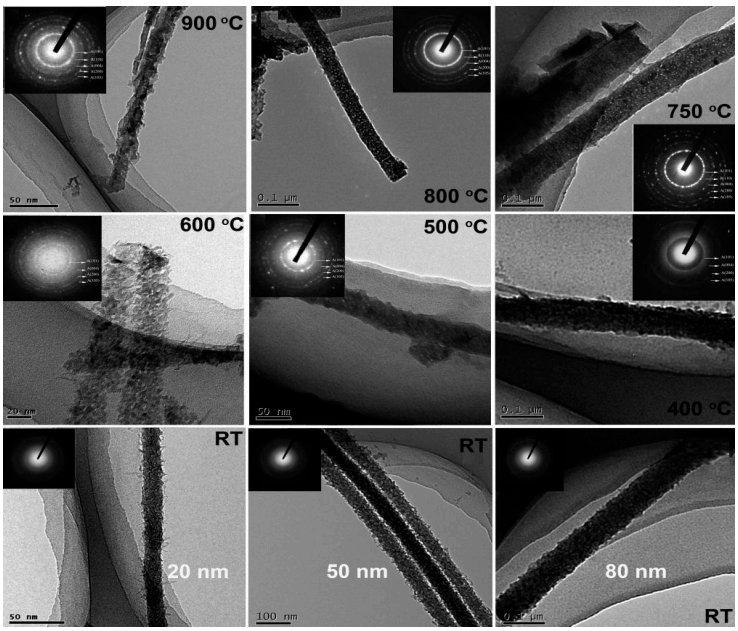

Figure 9. Typical TEM images of the as-prepared and annealed TiO_2 nanowires with diameters of 20, 50, and 80 nm. The insets show corresponding SAED patterns (reprinted from [16] with permission, Copyright Springer, 2012).

Peer-reviewed version available at Nanomaterials 2017, 7, 382; doi:10.3390/nano7110382

To quantitatively study the nucleation and growth kinetics, *in-situ* X-ray diffraction technique was employed to track the transformation process from anatase to rutile phase. Taken TiO_2-20 and TiO_2 powder for typical examples, the transformed rutile phase showed an exponential growth versus annealing time t, and the growth of the rutile was a thermally activated process (Figure 10). The rutile growth activation energy (E_g) values of 2.8±0.2 eV and 1.6±0.2 eV were determined in TiO_2-20 and TiO_2 power, respectively. Additionally, no obvious change of the rutile size was observed in the initial stage of the studied temperature range, indicating the increasing of the rutile volume fraction was induced by the nucleation events. By analyzing the dependence of nucleation rate on the annealing temperature, the rutile nucleation activation energy (E_n) values of 2.7±0.2 eV and 1.9±0.2 eV were yielded for TiO_2-20 and TiO_2 power, respectively. The higher nucleation and growth energy for TiO_2-20 implied

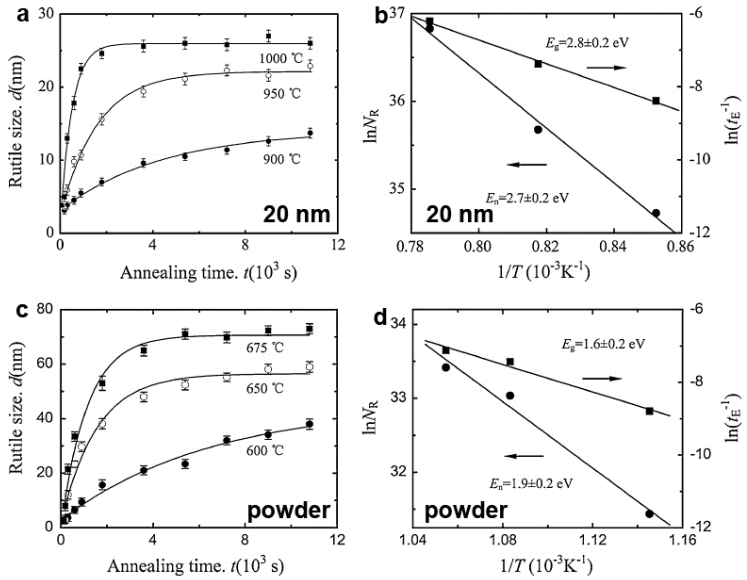

Figure 10. Nucleation and growth kinetics of nanocrystalline anatase to rutile. Annealing time dependence of the size of the rutile in the (a) nanowire and (c) free-state powders at different temperatures; Annealing temperature variations of the nucleation rate NR and the growth saturation rate t_E^{-1} for rutile in the (b) nanowire and (d) free-state powders, respectively (reprinted from [16] with permission, Copyright Springer, 2012).

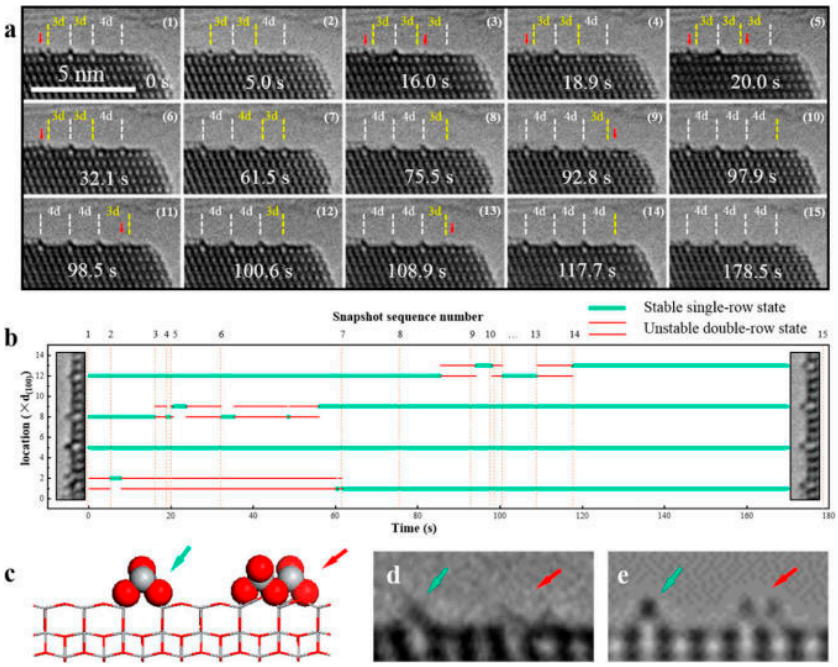

Figure 11. Atomic evolution of the (1×n) reconstructions on anatase TiO_2 (001) surface. (a) Sequential HRTEM images of the dynamic structural evolution, viewed from [010] direction, with the red arrows indicating the unstable states. (b) The statistical diagram of the locations of the TiO_x rows with green and red lines indicating the stable states and the unstable states. (c) Side view of the proposed model for the unstable two-row state with the TiO_x row shown as ball-and-stick (Ti, gray; O, red) on the TiO_2 stick framework. The green and red arrows indicate the stable single-row and instable doublerow structures, respectively. (d,e) Experimental HRTEM image compared with the simulated image based on the model in (c). (reprinted from [121] with permission, American Chemical Society, 2016)

the phase transformation from anatase to rutile was inhibited, i.e. the thermal stability of the anatase phase was improved. Our theoretical work showed the difference of thermal expansion coefficient between the nanoscale channel (aluminum oxide) and the embedded TiO_2 nanowire generated overpressure on the TiO_2/Al_2O_3 interface during annealing. The pressure can be estimated as ~0.13 GPa at 900 °C for TiO_2-20 sample. The pressure compressed the anatase surface and constrained the vibration of surface atoms, which were responsible for the improvement of the anatase phase. By choosing suitable surface layers and other coating techniques (such as Langmuir-Blodgett assembly, atomic layer deposition, etc), this surface/interface confinement strategy can also be used to improve the phase stability of other TiO_2 polymorphs. For example, Zazpe *et al*. recently reported on a very obvious enhancement of the phase stability of selforganized TiO_2 nanotubes layers with amorphous structure, provided by thin Al_2O_3 coatings of different thicknesses prepared by atomic layer deposition. TiO_2 nanotube layers coated with Al_2O_3 coatings exhibit significantly improved thermal stability as illustrated by the preservation of the nanotubular structure upon annealing treatment at high temperatures (870 °C) [15].

Besides phase transformation among the different TiO_2 polymorphs, surface atomic rearrangement (reconstruction) also occurs to achieve a more stable state at a certain environment (temperature, pressure, atmosphere, humidity, etc.). Remarkably different physical/chemical properties on the surface with respect to the bulk counterpart can be achieved by the reconstruction. Yuan *et al*. reported *in-situ* atomic scale environmental transmission electron microscopy observations of the formation and evolution of the (1 × 4) reconstruction dynamics on the anatase TiO_2 (001) surface under oxygen atmosphere. The real-time dynamics for the transition from metastable (1 × 3) and (1 × 5) to (1 × 4) and the unstable intermediate states were observed and identified (Figure 11). The special reconstruction was driven by the lowly coordinated atoms and

surface stress. The results demonstrate the power of *in situ* real-time technique to study the dynamic formation and evolution of surface structures.

5. Conclusions and Perspective

Recent years witness explosive research and development efforts on TiO_2 materials, ranging from controllable synthesis to advanced characterizations and device applications. Although the intrinsic properties such as wide bandgap, rapid carriers recombination, poor electronic conductivity, and coexistence of multiphases, hampered the practical applications of pristine TiO_2 materials to some extent, the surface/interface modifications have been demonstrated as effective routes to break the limitations, making it possible to be applied in diverse areas. This review article summarized the main progress in engineering the surface/interface structures in TiO_2 micro/nanostructures, discussed the effect of surface/interface structures on photocatalysis, lithium/sodium ion batteries, and Li-S batteries, and analyzed the phase transitions of TiO_2 nanostructures and possible strategies of improving the phase stability. Despite these impressive advances, several challenges still remain.

(1) Developing novel synthesis and treatment methods. Despite great success has been obtained in the controllable synthesis of TiO_2 nanostructures with tailored micro/nanostructures, there is still room for improvement in terms of quality of the products. Moreover, the new methods also provide opportunities to further understand the nucleation and growth.

(2) Control of the fine structures. High-index facets and defect sites are chemical active. However, the synthesis of TiO_2 nanocrystals with specific high-index facets is still a challenge. It is highly desirable to synthesize facet-controllable TiO_2 materials and further study the facet effect on energy storage, conversion and other applications. In addition, selectively generating defect structures and controlling their concentrations in different TiO_2 phases are significant to revel the role of defects in various physical and chemical processes.

(3) *In situ/operando* study the dynamic evolution of the surface/interface. *In situ/operando* spectroscopic or microscopic studies afford the chance to probe the evolution of TiO_2 surface/interface structures in working conditions, which is crucial to study the complex phase transformation and device stability.

Acknowledgments: This work was supported by Chinese National Natural Science Foundation (Grants No. 51401114, 51701063).

Conflicts of Interest: The authors declare no conflict of interest.

References

1. Sang, L.; Zhao, Y.; Burda, C. TiO_2 Nanoparticles as functional building blocks. *Chem. Rev.* **2014**, *114*, 9283–9318.
2. Liu, L.; Chen, X. Titanium dioxide nanomaterials: self-structural modifications. *Chem. Rev.* **2014**, *114*, 9890–9918.
3. Fujishima, A.; Honda, K. Electrochemical photolysis of water at a semiconductor electrode. *Nature* **1972**, *238*, 37–38.
4. Nolan, M.; Iwaszuk, A.; Lucid, A. K.; Carey, J. J.; Fronzi, M. Design of novel visible light activse photocatalyst materials: surface modified TiO_2. *Adv. Mater.* **2016**, *28*, 5425–5446.
5. Chen, X.; Liu, L.; Huang, F. Black titanium dioxide (TiO_2) nanomaterials. *Chem. Soc. Rev.* **2015**, *44*, 1861–1885.
6. Cargnello, M.; Gordon, T. R.; Murray, C. B. Solution-phase synthesis of titanium dioxide nanoparticles and nanocrystals. *Chem. Rev.* **2014**, *114*, 9319–9345.
7. Bai, Y.; Mora-Seró, I.; De Angelis, F.; Bisquert, J.; Wang, P. Titanium dioxide nanomaterials for photovoltaic applications. *Chem. Rev.* **2014**, *114*, 10095–10130.
8. Ma, Y.; Wang, X.; Jia, Y.; Chen, X.; Han, H.; Li, C. Titanium dioxide-based nanomaterials for photocatalytic fuel generations. *Chem. Rev.* **2014**, *114*, 9987–10043.
9. Asahi, R.; Morikawa, T.; Irie, H.; Ohwaki, T. Nitrogen-doped titanium dioxide as visible-light-sensitive photocatalyst: designs, developments, and prospects. *Chem. Rev.* **2014**, *114*, 9824–9852.

10. Kapilashrami, M.; Zhang, Y.; Liu, Y.-S.; Hagfeldt, A.; Guo, J. Probing the optical property and electronic structure of TiO_2 nanomaterials for renewable energy applications. *Chem. Rev.* **2014**, *114*, 9662–9707.
11. Schneider, J.; Matsuoka, M.; Takeuchi, M.; Zhang, J.; Horiuchi, Y.; Anpo, M.; Bahnemann, D. W. Understanding TiO_2 photocatalysis: mechanisms and materials. *Chem. Rev.* **2014**, *114*, 9919–9986.
12. Ferrighi, L.; Datteo, M.; Fazio, G.; Di Valentin, C. Catalysis under cover: enhanced reactivity at the interface between (doped) graphene and anatase TiO_2. *J. Am. Chem. Soc.* **2016**, *138*, 7365–7376.
13. Bourikas, K.; Kordulis, C.; Lycourghiotis, A. Titanium dioxide (anatase and rutile): surface chemistry, liquid–solid interface chemistry, and scientific synthesis of supported catalysts. *Chem. Rev.* **2014**, *114*, 9754–9823.
14. Hua, X.; Liu, Z.; Bruce, P. G.; Grey, C. P. The morphology of TiO_2(B) nanoparticles. *J. Am. Chem. Soc.* **2015**, *137*, 13612–13623.
15. Zazpe, R.; Prikryl, J.; Gärtnerova, V.; Nechvilova, K.; Benes, L.; Strizik, L.; Jäger, A.; Bosund, M.; Sopha, H.; Macak, J. M. Atomic layer deposition Al_2O_3 coatings significantly improve thermal, chemical, and mechanical stability of anodic TiO_2 nanotube layers. *Langmuir* **2017**, *33*, 3208–3216.
16. Wang, X. Enhancement of thermal stability of TiO_2 nanowires embedded in anodic aluminum oxide template. *J. Mater. Sci.* **2012**, *47*, 739–745.
17. Zhou, W.; Sun, F.; Pan, K.; Tian, G.; Jiang, B.; Ren, Z.; Tian, C.; Fu, H. Well-ordered large-pore mesoporous anatase TiO_2 with remarkably high thermal stability and improved crystallinity: preparation, characterization, and photocatalytic performance. *Adv. Funct. Mater.* **2011**, *21*, 1922–1930.
18. Biswas, D.; Biswas, J.; Ghosh, S.; Wood, B.; Lodha, S. Enhanced thermal stability of Ti/TiO_2/n-Ge contacts through plasma nitridation of TiO_2 interfacial layer. *Appl. Phys. Lett*. **2017**, 110, 052104/1–5.
19. Liu, G.; Yang, H. G.; Pan, J.; Yang, Y. Q.; Lu, G. Q. (Max); Cheng, H.-M. Titanium dioxide crystals with tailored facets. *Chem. Rev.* **2014**, *114*, 9559–9612.
20. Wang, Y.; Sun, H.; Tan, S.; Feng, H.; Cheng, Z.; Zhao, J.; Zhao, A.; Wang, B.; Luo, Y.; Yang, J.; Hou, J. G. Role of point defects on the reactivity of reconstructed anatase titanium dioxide (001) surface. *Nat. Commun.* **2013**, *4*, 2214/1–8.
21. Sun, R.; Wang, Z.; Saito, M.; Shibata, N.; Ikuhara, Y. Atomistic mechanisms of nonstoichiometry-induced twin boundary structural transformation in titanium dioxide. *Nat. Commun.* **2015**, *6*, 7120/1–7.
22. Selcuk, S.; Selloni, A. Facet-dependent trapping and dynamics of excess electrons at anatase TiO_2 surfaces and aqueous interfaces. *Nat. Mater.* **2016**, *15*, 1107–1112.
23. Zhang, X.; He, Y.; Sushko, M. L.; Liu, J.; Luo, L.; Yoreo, J. J. D.; Mao, S. X.; Wang, C.; Rosso, K. M. Direction-specific van der Waals attraction between rutile TiO_2 nanocrystals. *Science* **2017**, *356*, 434–437.
24. Longoni, G.; Pena Cabrera, R. L.; Polizzi, S.; D'Arienzo, M.; Mari, C. M.; Cui, Y.; Ruffo, R. Shape-controlled TiO_2 nanocrystals for Na-ion battery electrodes: the role of different exposed crystal facets on the electrochemical properties. *Nano Lett.* **2017**, *17*, 992–1000.
25. Li, Z.; Zhang, J.; Guan, B.; Wang, D.; Liu, L.-M.; Lou, X. W. (David). A sulfur host based on titanium monoxide@carbon hollow spheres for advanced lithium–sulfur batteries. *Nat. Commun.* **2016**, *7*, 13065/1–11.
26. Setvín, M.; Aschauer, U.; Scheiber, P.; Li, Y.-F.; Hou, W.; Schmid, M.; Selloni, A.; Diebold, U. Reaction of O_2 with subsurface oxygen vacancies on TiO_2 anatase (101). *Science* **2013**, *341*, 988–991.
27. Zhou, P.; Zhang, H.; Ji, H.; Ma, W.; Chen, C.; Zhao, J. Modulating the photocatalytic redox preferences between anatase TiO_2 {001} and {101} surfaces. *Chem. Commun.* **2017**, *53*, 787–790.
28. Yang, H. G.; Sun, C. H.; Qiao, S. Z.; Zou, J.; Liu, G.; Smith, S. C.; Cheng, H. M.; Lu, G. Q. Anatase TiO_2 single crystals with a large percentage of reactive facets. *Nature* **2008**, *453*, 638–641.
29. Crossland, E. J. W.; Noel, N.; Sivaram, V.; Leijtens, T.; Alexander-Webber, J. A.; Snaith, H. J. Mesoporous TiO_2 single crystals delivering enhanced mobility and optoelectronic device performance. *Nature* **2013**, *495*, 215–219.
30. Pabón, B. M.; Beltrán, J. I.; Sánchez-Santolino, G.; Palacio, I.; López-Sánchez, J.; Rubio-Zuazo, J.; Rojo, J. M.; Ferrer, P.; Mascaraque, A.; Muñoz, M. C.; Varela, M.; Castro, G. R.; de la Fuente, O. R. Formation of titanium monoxide (001) single-crystalline thin film induced by ion bombardment of titanium dioxide (110). *Nat. Commun.* **2015**, *6*, 6147/1–6.
31. Wang, X.; Li, Z.; Shi, J.; Yu, Y. One-dimensional titanium dioxide nanomaterials: nanowires, nanorods, and nanobelts. *Chem. Rev.* **2014**, *114*, 9346–9384.

32. Richter, C.; Schmuttenmaer, C. A. Exciton-like trap states limit electron mobility in TiO_2 nanotubes. *Nat. Nanotechnol.* **2010**, *5*, 769–772.
33. Penn, R. L.; Banfield, J. F. Morphology development and crystal growth in nanocrystalline aggregates under hydrothermal conditions: insights from titania. *Geochim. Cosmochim. Ac.* **1999**, *63*, 1549–1557.
34. Chen, X.; Liu, L.; Yu, P. Y.; Mao, S. S. Increasing solar absorption for photocatalysis with black hydrogenated titanium dioxide nanocrystals. *Science* **2011**, *331*, 746–750.
35. Huang, J.; Fang, F.; Huang, G.; Sun, H.; Zhu, J.; Yu, R. Engineering the surface of rutile TiO_2 nanoparticles with quantum pits towards excellent lithium storage. *RSC Adv.* **2016**, *6*, 66197–66203.
36. Jiménez, J. M.; Bourret, G. R.; Berger, T.; McKenna, K. P. Modification of charge trapping at particle/particle interfaces by electrochemical hydrogen doping of nanocrystalline TiO_2. *J. Am. Chem. Soc.* **2016**, *138*, 15956–15964.
37. Giordano, F.; Abate, A.; Correa Baena, J. P.; Saliba, M.; Matsui, T.; Im, S. H.; Zakeeruddin, S. M.; Nazeeruddin, M. K.; Hagfeldt, A.; Graetzel, M. Enhanced electronic properties in mesoporous TiO_2 via lithium doping for high-efficiency perovskite solar cells. *Nat. Commun.* **2016**, *7*, 10379/1–6.
38. Ide, Y.; Inami, N.; Hattori, H.; Saito, K.; Sohmiya, M.; Tsunoji, N.; Komaguchi, K.; Sano, T.; Bando, Y.; Golberg, D.; Sugahara, Y. Remarkable charge separation and photocatalytic efficiency enhancement through interconnection of TiO_2 nanoparticles by hydrothermal treatment. *Angew. Chem. Int. Ed.* **2016**, *55*, 3600–3605.
39. Liu, J.; Olds, D.; Peng, R.; Yu, L.; Foo, G. S.; Qian, S.; Keum, J.; Guiton, B. S.; Wu, Z.; Page, K. Quantitative analysis of the morphology of {101} and {001} faceted anatase TiO_2 nanocrystals and its implication on photocatalytic activity. *Chem. Mater.* **2017**, *29*, 5591–5604.
40. Li, W.; Wu, Z.; Wang, J.; Elzatahry, A. A.; Zhao, D. A Perspective on mesoporous TiO_2 materials. *Chem. Mater.* **2014**, *26*, 287–298.
41. Raghunath, P.; Huang, W. F.; Lin, M. C. Quantum chemical elucidation of the mechanism for hydrogenation of TiO_2 anatase crystals. *J. Chem. Phys.* **2013**, *138*, 154705/1–9.
42. Pan, H.; Zhang, Y.-W.; Shenoy, V. B.; Gao, H. Effects of H-, N-, and (H, N)-doping on the photocatalytic activity of TiO_2. *J. Phys. Chem. C* **2011**, *115*, 12224–12231.
43. Aschauer, U.; Selloni, A. Hydrogen interaction with the anatase TiO_2 (101) surface. *Phys. Chem. Chem. Phys.* **2012**, *14*, 16595–16602.
44. Li, X.; Yu, J.; Jaroniec, M. Hierarchical photocatalysts. *Chem. Soc. Rev.* **2016**, *45*, 2603–2636.
45. Yu, J.; Low, J.; Xiao, W.; Zhou, P.; Jaroniec, M. Enhanced photocatalytic CO_2-reduction activity of Anatase TiO_2 by coexposed {001} and {101} Facets. *J. Am. Chem. Soc.* **2014**, 136, 8839–8842.
46. Low, J.; Cheng, B.; Yu, J. Surface modification and enhanced photocatalytic CO_2 reduction performance of TiO_2 : a review. *Appl. Surf. Sci.* **2017**, 392, 658–686.
47. Li, J.; Zhang, M.; Guan, Z.; Li, Q.; He, C.; Yang, J. Synergistic effect of surface and bulk single-electron-trapped oxygen vacancy of TiO_2 in the photocatalytic reduction of CO_2. *Appl. Catal. B: Environ.* **2017**, *206*, 300–307.
48. Edy, R.; Zhao, Y.; Huang, G. S.; Shi, J. J.; Zhang, J.; Solovev, A. A.; Mei, Y. TiO_2 nanosheets synthesized by atomic layer deposition for photocatalysis. *Prog. Nat. Sci.* **2016**, *26*, 493–497.
49. Wang, X.; He, H.; Chen, Y.; Zhao, J.; Zhang, X. Anatase TiO_2 hollow microspheres with exposed {001} facets: facile synthesis and enhanced photocatalysis. *Appl. Surf. Sci.* **2012**, *258*, 5863–5868.
50. Xiang, Q.; Yu, J. Photocatalytic activity of hierarchical flower-like TiO_2 superstructures with dominant {001} facets. *Chin. J. Catal.* **2011**, 32, 525–531.
51. Cao, Y.; Xing, Z.; Shen, Y.; Li, Z.; Wu, X.; Yan, X.; Zou, J.; Yang, S.; Zhou, W. Mesoporous black Ti^{3+}/N-TiO_2 spheres for efficient visible-light-driven photocatalytic performance. *Chem. Eng. J.* **2017**, *325*, 199–207.
52. An, X.; Zhang, L.; Wen, B.; Gu, Z.; Liu, L.-M.; Qu, J.; Liu, H. Boosting photoelectrochemical activities of heterostructured photoanodes through interfacial modulation of oxygen vacancies. *Nano Energy* **2017**, *35*, 290–298.
53. Chen, Y.; Li, W.; Wang, J.; Gan, Y.; Liu, L.; Ju, M. Microwave-assisted ionic liquid synthesis of Ti^{3+} self-doped TiO_2 hollow nanocrystals with enhanced visible-light photoactivity. *Appl. Catal. B: Environ.* **2016**, *191*, 94–105.
54. Shuang, S.; Lv, R.; Xie, Z.; Zhang, Z. Surface plasmon enhanced photocatalysis of Au/Pt-decorated TiO_2 nanopillar arrays. *Sci. Rep.* **2016**, *6*, 26670/1–8.

55. Chiu, Y.-H.; Hsu, Y.-J. Au@Cu_7S_4 yolk@shell nanocrystal-decorated TiO_2 nanowires as an all-day-active photocatalyst for environmental purification. *Nano Energy* **2017**, *31*, 286–295.
56. Jin, J.; Wang, C.; Ren, X.-N.; Huang, S.-Z.; Wu, M.; Chen, L.-H.; Hasan, T.; Wang, B.-J.; Li, Y.; Su, B.-L. Anchoring ultrafine metallic and oxidized Pt nanoclusters on yolk-shell TiO_2 for unprecedentedly high photocatalytic hydrogen production. *Nano Energy* **2017**, *38*, 118–126.
57. Yu, C.; Yu, Y.; Xu, T.; Wang, X.; Ahmad, M.; Sun, H. Hierarchical nanoflowers assembled with Au nanoparticles decorated ZnO nanosheets toward enhanced photocatalytic properties. *Mate. Lett.* **2017**, *190*, 185–187.
58. Wu, T.; Kang, X.; Kadi, M. W.; Ismail, I.; Liu, G.; Cheng, H.-M. Enhanced photocatalytic hydrogen generation of mesoporous rutile TiO_2 single crystal with wholly exposed {111} facets. *Chin. J. Catal.* **2015**, 36, 2103–2108.
59. Zhang, K.; Liu, Q.; Wang, H.; Zhang, R.; Wu, C.; Gong, J. R. TiO_2 single crystal with four-truncated-bipyramid morphology as an efficient photocatalyst for hydrogen production. *Small* **2013**, 9, 2452–2459.
60. Hu, J.; Cao, Y.; Wang, K.; Jia, D. Green solid-state synthesis and photocatalytic hydrogen production activity of anatase TiO_2 nanoplates with super heat-stability. *RSC Adv.* **2017**, 7, 11827–11833.
61. Wu, Q.; Huang, F.; Zhao, M.; Xu, J.; Zhou, J.; Wang, Y. Ultra-small yellow defective TiO_2 nanoparticles for co-catalyst free photocatalytic hydrogen production. *Nano Energy* **2016**, *24*, 63–71.
62. Pei, D.-N.; Gong, L.; Zhang, A.-Y.; Zhang, X.; Chen, J.-J.; Mu, Y.; Yu, H.-Q. Defective titanium dioxide single crystals exposed by high-energy {001} facets for efficient oxygen reduction. *Nat. Commun.* **2015**, *6*, 8696/1–10.
63. Yang, Y.; Gao, P.; Wang, Y.; Sha, L.; Ren, X.; Zhang, J.; Chen, Y.; Wu, T.; Yang, P.; Li, X. A direct charger transfer from interface to surface for the highly efficient spatial separation of electrons and holes: The construction of Ti–C bonded interfaces in TiO_2-C composite as a touchstone for photocatalytic water splitting. *Nano Energy* **2017**, *33*, 29–36.
64. Gao, L.; Li, Y.; Ren, J.; Wang, S.; Wang, R.; Fu, G.; Hu, Y. Passivation of defect states in anatase TiO_2 hollow spheres with Mg doping: Realizing efficient photocatalytic overall water splitting. *Appl. Catal. B: Environ.* **2017**, *202*, 127–133.
65. Yang, Y.; Liu, G.; Irvine, J. T. S.; Cheng, H.-M. Enhanced photocatalytic H_2 production in core-shell engineered rutile TiO_2. *Adv. Mater.* **2016**, *28*, 5850–5856.
66. Wu, B.; Liu, D.; Mubeen, S.; Chuong, T. T.; Moskovits, M.; Stucky, G. D. Anisotropic growth of TiO_2 onto gold nanorods for plasmon-enhanced hydrogen production from water reduction. *J. Am. Chem. Soc.* **2016**, *138*, 1114–1117.
67. Lee, C.-Y.; Park, H. S.; Fontecilla-Camps, J. C.; Reisner, E. Photoelectrochemical H_2 evolution with a hydrogenase immobilized on a TiO_2-protected silicon electrode. *Angew. Chem. Int. Ed. Engl.* **2016**, *55*, 5971–5974.
68. Valenti, G.; Boni, A.; Melchionna, M.; Cargnello, M.; Nasi, L.; Bertoni, G.; Gorte, R. J.; Marcaccio, M.; Rapino, S.; Bonchio, M.; Fornasiero, P.; Prato, M.; Paolucci, F. Co-axial heterostructures integrating palladium/titanium dioxide with carbon nanotubes for efficient electrocatalytic hydrogen evolution. *Nat. Commun.* **2016**, *7*, 13549/1–8.
69. Zhang, R.; Shao, M.; Xu, S.; Ning, F.; Zhou, L.; Wei, M. Photo-assisted synthesis of zinc-iron layered double hydroxides/TiO_2 nanoarrays toward highly-efficient photoelectrochemical water splitting. *Nano Energy* **2017**, *33*, 21–28.
70. Bendova, M.; Gispert-Guirado, F.; Hassel, A. W.; Llobet, E.; Mozalev, A. Solar water splitting on porous-alumina-assisted TiO_2-doped WO_x nanorod photoanodes: Paradoxes and challenges. *Nano Energy* **2017**, *33*, 72–87.
71. Yue, X.; Yi, S.; Wang, R.; Zhang, Z.; Qiu, S. A novel architecture of dandelion-like Mo_2C/TiO_2 heterojunction photocatalysts towards high-performance photocatalytic hydrogen production from water splitting. *J. Mater. Chem. A* **2017**, *5*, 10591–10598.
72. He, H.; Lin, J.; Fu, W.; Wang, X.; Wang, H.; Zeng, Q.; Gu, Q.; Li, Y.; Yan, C.; Tay, B. K.; Xue, C.; Hu, X.; Pantelides, S. T.; Zhou, W.; Liu, Z. MoS_2/TiO_2 edge-on heterostructure for efficient photocatalytic hydrogen evolution. *Adv. Energy Mater.* **2016**, *6*, 1600464/1–7.

73. Abdellah, M.; El-Zohry, A. M.; Antila, L. J.; Windle, C. D.; Reisner, E.; Hammarström, L. Time-resolved IR spectroscopy reveals a mechanism with TiO_2 as a reversible electron acceptor in a TiO_2–Re catalyst system for CO_2 photoreduction. *J. Am. Chem. Soc.* **2017**, *139*, 1226–1232.
74. Matsubu, J. C.; Zhang, S.; DeRita, L.; Marinkovic, N. S.; Chen, J. G.; Graham, G. W.; Pan, X.; Christopher, P. Adsorbate-mediated strong metal–support interactions in oxide-supported Rh catalysts. *Nat. Chem.* **2016**, *9*, 120–127.
75. Bumajdad, A.; Madkour, M. Understanding the superior photocatalytic activity of noble metals modified titania under UV and visible light irradiation. *Phys. Chem. Chem. Phys.* **2014**, *16*, 7146–7158.
76. Grigioni, I.; Dozzi, M. V.; Bernareggi, M.; Chiarello, G. L.; Selli, E. Photocatalytic CO_2 reduction vs. H_2 production: the effects of surface carbon-containing impurities on the performance of TiO_2-based photocatalysts. *Catal. Today* **2017**, *281*, 214–220.
77. Truong, Q. D.; Hoa, H. T.; Le, T. S. Rutile TiO_2 nanocrystals with exposed {331} facets for enhanced photocatalytic CO_2 reduction activity. *J. Colloid Interf. Sci.* **2017**, *504*, 223–229.
78. Yang, X.; Qian, X.; Jin, L.; Zhao, D.; Wang, S.; Rao, D.; Yao, S.; Shen, X.; Zhou, Y.; Xi, X. Mesoporous TiO_2 nanosheet with a large amount of exposed {001} facets as sulfur host for high-performance lithium–sulfur batteries. *J. Solid State Electrochem.* **2016**, *20*, 2161–2168.
79. Yu, Y.; Wang, X.; Sun, H.; Ahmad, M. 3D anatase TiO_2 hollow microspheres assembled with high-energy {001} facets for lithium-ion batteries. *RSC Adv.* **2012**, *2*, 7901–7905.
80. Gao, X.; Li, G.; Xu, Y.; Hong, Z.; Liang, C.; Lin, Z. TiO_2 Microboxes with controlled internal porosity for high-performance lithium storage. *Angew. Chem. Int. Ed. Engl.* **2015**, *54*, 14331–14335.
81. McNulty, D.; Carroll, E.; O'Dwyer, C. Rutile TiO_2 inverse opal anodes for li-ion batteries with long cycle life, high-rate capability, and high structural stability. *Adv. Energy Mater.* **2017**, *7*, 1602291/1–8.
82. Liu, G.; Yin, L.-C.; Pan, J.; Li, F.; Wen, L.; Zhen, C.; Cheng, H.-M. Greatly enhanced electronic conduction and lithium storage of faceted TiO_2 crystals supported on metallic substrates by tuning crystallographic orientation of TiO_2. *Adv. Mater.* **2015**, *27*, 3507–3512.
83. Liu, S.; Jia, H.; Han, L.; Wang, J.; Gao, P.; Xu, D.; Yang, J.; Che, S. Nanosheet-constructed porous TiO_2-B for advanced lithium ion batteries. *Adv. Mater.* **2012**, *24*, 3201–3204.
84. Gao, R.; Jiao, Z.; Wang, Y.; Xu, L.; Xia, S.; Zhang, H. Eco-friendly synthesis of rutile TiO_2 nanostructures with controlled morphology for efficient lithium-ion batteries. *Chem. Eng. J.* **2016**, *304*, 156–164.
85. Wang, Z.; Zhang, F.; Xing, H.; Gu, M.; An, J.; Zhai, B.; An, Q.; Yu, C.; Li, G. Fabrication of nest-like TiO_2 hollow microspheres and its application for lithium ion batteries with high-rate performance. *Electrochim. Acta* **2017**, *243*, 112–118.
86. Mujtaba, J.; Sun, H.; Zhao, Y.; Xiang, G.; Xu, S.; Zhu, J. High-performance lithium storage based on the synergy of atomic-thickness nanosheets of TiO_2(B) and ultrafine Co_3O_4 nanoparticles. *J. Power Sources* **2017**, *363*, 110–116.
87. Cao, M.; Gao, L.; Lv, X.; Shen, Y. TiO_2-B@VS_2 heterogeneous nanowire arrays as superior anodes for lithium-ion batteries. *J. Power Sources* **2017**, *350*, 87–93.
88. Lan, T.; Zhang, W.; Wu, N.-L.; Wei, M. Nb-doped rutile TiO_2 mesocrystals with enhanced lithium storage properties for lithium ion battery. *Chem.-Eur. J.* **2017**, *23*, 5059–5065.
89. Chen, B.; Liu, E.; He, F.; Shi, C.; He, C.; Li, J.; Zhao, N. 2D sandwich-like carbon-coated ultrathin TiO_2@defect-rich MoS_2 hybrid nanosheets: synergistic-effect-promoted electrochemical performance for lithium ion batteries. *Nano Energy* **2016**, *26*, 541–549.
90. Chen, B.; Liu, E.; Cao, T.; He, F.; Shi, C.; He, C.; Ma, L.; Li, Q.; Li, J.; Zhao, N. Controllable graphene incorporation and defect engineering in MoS_2-TiO_2 based composites: towards high-performance lithium-ion batteries anode materials. *Nano Energy* **2017**, *33*, 247–256.
91. Lui, G.; Li, G.; Wang, X.; Jiang, G.; Lin, E.; Fowler, M.; Yu, A.; Chen, Z. Flexible, three-dimensional ordered macroporous TiO_2 electrode with enhanced electrode–electrolyte interaction in high-power Li-ion batteries. *Nano Energy* **2016**, *24*, 72–77.
92. Jin, J.; Huang, S.-Z.; Shu, J.; Wang, H.-E.; Li, Y.; Yu, Y.; Chen, L.-H.; Wang, B.-J.; Su, B.-L. Highly porous TiO_2 hollow microspheres constructed by radially oriented nanorods chains for high capacity, high rate and long cycle capability lithium battery. *Nano Energy* **2015**, *16*, 339–349.
93. Li, X.; Wu, G.; Liu, X.; Li, W.; Li, M. Orderly integration of porous TiO_2(B) nanosheets into bunchy hierarchical structure for high-rate and ultralong-lifespan lithium-ion batteries. *Nano Energy* **2017**, *31*, 1–8.

94. Ren, G.; Hoque, M. N. F.; Liu, J.; Warzywoda, J.; Fan, Z. Perpendicular edge oriented graphene foam supporting orthogonal TiO_2(B) nanosheets as freestanding electrode for lithium ion battery. *Nano Energy* **2016**, *21*, 162–171.
95. Liu, Y.; Elzatahry, A. A.; Luo, W.; Lan, K.; Zhang, P.; Fan, J.; Wei, Y.; Wang, C.; Deng, Y.; Zheng, G.; Zhang, F.; Tang, Y.; Mai, L.; Zhao, D. Surfactant-templating strategy for ultrathin mesoporous TiO_2 coating on flexible graphitized carbon supports for high-performance lithium-ion battery. *Nano Energy* **2016**, *25*, 80–90.
96. Wang, S.; Yang, Y.; Quan, W.; Hong, Y.; Zhang, Z.; Tang, Z.; Li, J. Ti^{3+}-free three-phase $Li_4Ti_5O_{12}/TiO_2$ for high-rate lithium ion batteries: capacity and conductivity enhancement by phase boundaries. *Nano Energy* **2017**, *32*, 294–301.
97. Mao, M.; Yan, F.; Cui, C.; Ma, J.; Zhang, M.; Wang, T.; Wang, C. Pipe-wire TiO_2–Sn@carbon nanofibers paper anodes for lithium and sodium ion batteries. *Nano Lett.* **2017**, *17*, 3830–3836.
98. Wang, N.; Bai, Z.; Qian, Y.; Yang, J. Double-Walled Sb@TiO_{2-x} Nanotubes as a superior high-rate and ultralong-lifespan anode material for Na-ion and Li-ion batteries. *Adv. Mater.* **2016**, *28*, 4126–4133.
99. Tahir, M. N.; Oschmann, B.; Buchholz, D.; Dou, X.; Lieberwirth, I.; Panthöfer, M.; Tremel, W.; Zentel, R.; Passerini, S. Extraordinary performance of carbon-coated anatase TiO_2 as sodium-ion anode. *Adv. Energy Mater.* **2016**, *6*, 1501489/1–9.
100. Ni, J.; Fu, S.; Wu, C.; Maier, J.; Yu, Y.; Li, L. Self-supported nanotube arrays of sulfur-doped TiO_2 enabling ultrastable and robust sodium storage. *Adv. Mater.* **2016**, *28*, 2259–2265.
101. Zhou, M.; Xu, Y.; Wang, C.; Li, Q.; Xiang, J.; Liang, L.; Wu, M.; Zhao, H.; Lei, Y. Amorphous TiO_2 inverse opal anode for high-rate sodium ion batteries. *Nano Energy* **2017**, *31*, 514–524.
102. Zhang, Y.; Foster, C. W.; Banks, C. E.; Shao, L.; Hou, H.; Zou, G.; Chen, J.; Huang, Z.; Ji, X. Graphene-rich wrapped petal-like rutile TiO_2 tuned by carbon dots for high-performance sodium storage. *Adv. Mater.* **2016**, *28*, 9391–9399.
103. Zhang, Y.; Wang, C.; Hou, H.; Zou, G.; Ji, X. Nitrogen doped/carbon tuning yolk-like TiO_2 and its remarkable impact on sodium storage performances. *Adv. Energy Mater.* **2017**, *7*, 1600173/1–12.
104. Chu, S.; Zhong, Y.; Cai, R.; Zhang, Z.; Wei, S.; Shao, Z. Mesoporous and nanostructured TiO_2 layer with ultra-high loading on nitrogen-doped carbon foams as flexible and free-standing electrodes for lithium-ion batteries. *Small* **2016**, *12*, 6724–6734.
105. Reddy, M. A.; Kishore, M. S.; Pralong, V.; Varadaraju, U. V.; Raveau, B. Lithium Intercalation into Nanocrystalline Brookite TiO_2. *Electrochem. Solid-State Lett.* **2007**, *10*, A29–A31.
106. Jamnik, J.; Maier, J. Nanocrystallinity effects in lithium battery materials Part IV. *Phys. Chem. Chem. Phys.* **2003**, *5*, 5215–5220.
107. Wu, Q.; Xu, J.; Yang, X.; Lu, F.; He, S.; Yang, J.; Fan, H. J.; Wu, M. Ultrathin anatase TiO_2 nanosheets embedded with TiO_2-B nanodomains for lithium-ion storage: capacity enhancement by phase boundaries. *Adv. Energy Mate.* **2015**, *5*, 1401756/1–9.
108. Zhang, Y.; Ding, Z.; Foster, C. W.; Banks, C. E.; Qiu, X.; Ji, X. Oxygen vacancies evoked blue TiO_2(B) nanobelts with efficiency enhancement in sodium storage behaviors. *Adv. Funct. Mater.* **2017**, *27*, 1700856/1–12.
109. Pang, Q.; Kundu, D.; Cuisinier, M.; Nazar, L. F. Surface-enhanced redox chemistry of polysulphides on a metallic and polar host for lithium-sulphur batteries. *Nat. Commun.* **2014**, *5*, 4759/1–8.
110. Yu, M.; Ma, J.; Song, H.; Wang, A.; Tian, F.; Wang, Y.; Qiu, H.; Wang, R. Atomic layer deposited TiO_2 on a nitrogen-doped graphene/sulfur electrode for high performance lithium–sulfur batteries. *Energy Environ. Sci.* **2016**, *9*, 1495–1503.
111. Wei Seh, Z.; Li, W.; Cha, J. J.; Zheng, G.; Yang, Y.; McDowell, M. T.; Hsu, P.-C.; Cui, Y. Sulphur–TiO_2 yolk–shell nanoarchitecture with internal void space for long-cycle lithium–sulphur batteries. *Nat. Commun.* **2013**, *4*, 1331/1–6.
112. Song, X.; Gao, T.; Wang, S.; Bao, Y.; Chen, G.; Ding, L.-X.; Wang, H. Free-standing sulfur host based on titanium-dioxide-modified porous-carbon nanofibers for lithium-sulfur batteries. *J. Power Sources* **2017**, *356*, 172–180.
113. Liang, G.; Wu, J.; Qin, X.; Liu, M.; Li, Q.; He, Y.-B.; Kim, J.-K.; Li, B.; Kang, F. Ultrafine TiO_2 decorated carbon nanofibers as multifunctional interlayer for high-performance lithium–sulfur battery. *ACS Appl. Mater. Inter.* **2016**, *8*, 23105–23113.

114. Xiao, Z.; Yang, Z.; Wang, L.; Nie, H.; Zhong, M.; Lai, Q.; Xu, X.; Zhang, L.; Huang, S. A lightweight TiO_2/graphene interlayer, applied as a highly effective polysulfide absorbent for fast, long-life lithium-sulfur batteries. *Adv. Mater.* **2015**, *27*, 2891–2898.
115. Mei, S.; Jafta, C. J.; Lauermann, I.; Ran, Q.; Kärgell, M.; Ballauff, M.; Lu, Y. Porous Ti_4O_7 particles with interconnected-pore structure as a high-efficiency polysulfide mediator for lithium-sulfur batteries. *Adv. Funct. Mater.* **2017**, *27*, 1701176/1–10.
116. Zhao, Y.; Zhu, W.; Chen, G. Z.; Cairns, E. J. Polypyrrole/TiO_2 nanotube arrays with coaxial heterogeneous structure as sulfur hosts for lithium sulfur batteries. *J. Power Sources* **2016**, *327*, 447–456.
117. Huang, J.-Q.; Wang, Z.; Xu, Z.-L.; Chong, W. G.; Qin, X.; Wang, X.; Kim, J.-K. Three-dimensional porous graphene aerogel cathode with high sulfur loading and embedded TiO_2 nanoparticles for advanced lithium–sulfur batteries. *ACS Appl. Mater. Inter.* **2016**, *8*, 28663–28670.
118. Zhou, G.; Zhao, Y.; Zu, C.; Manthiram, A. Free-standing TiO_2 nanowire-embedded graphene hybrid membrane for advanced Li/dissolved polysulfide batteries. *Nano Energy* **2015**, *12*, 240–249.
119. Ding, B.; Xu, G.; Shen, L.; Nie, P.; Hu, P.; Dou, H.; Zhang, X. Fabrication of a sandwich structured electrode for high-performance lithium–sulfur batteries. *J. Mater. Chem. A* **2013**, *1*, 14280–14285.
120. Zhang, H.; Banfield, J. F. Structural Characteristics and mechanical and thermodynamic properties of nanocrystalline TiO_2. *Chem. Rev.* **2014**, *114*, 9613–9644.
121. Yuan, W.; Wang, Y.; Li, H.; Wu, H.; Zhang, Z.; Selloni, A.; Sun, C. Real-time observation of reconstruction Dynamics on TiO_2(001) surface under oxygen via an environmental transmission electron microscope. *Nano Lett.* **2016**, *16*, 132–137.